Quantitative and Regional Analysis of Lung Function Assessed by Hyperpolarized Xe-129 MRI

A Thesis

Presented to

the faculty of the School of Engineering and Applied Science

University of Virginia

---

in partial fulfillment
of the requirements for the degree

Master of Science

by

Zixuan Lin

May 2019

APPROVAL SHEET

This Thesis
is submitted in partial fulfillment of the requirements
for the degree of
Master of Science

Author Signature: 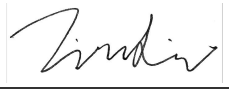

This Thesis has been read and approved by the examining committee:

Advisor: Kun Qing

Committee Member: Craig H. Meyer

Committee Member: Y. Michael Shim

Committee Member: _____

Committee Member: _____

Committee Member: _____

Accepted for the School of Engineering and Applied Science:

Craig H. Benson, School of Engineering and Applied Science

May 2019

Abstract

Lungs handle human gas exchange with atmosphere through respiration, bringing in oxygen required by cell metabolism, and expelling carbon dioxide containing wastes of the body. Nowadays, more and more people suffer from respiratory disorders. In 2016, chronic lower respiratory diseases were the 4th leading cause of death in the United States, with more than 150 thousand people dying from them, and millions more suffering from them without being diagnosed [1].

Under this situation, effective techniques for assessing lung function are strongly desired. Conventional techniques being used in clinic include pulmonary function tests (e.g., spirometry, lung volumes, quantitation of diffusing capacity for carbon monoxide) and radiological imaging (e.g., chest X-ray, chest CT). However, their lack of regional or functional information limits their application. Quantitative techniques with the ability to provide regional information of lung structure and function are valuable in lung disease diagnosis and treatment.

Hyperpolarized gas (HPG) MRI, as it provides the image of lung structure and function with high spatial and temporal resolution, gives an opportunity to quantitatively and regionally assess lung function. Hyperpolarized Xenon-129 ventilation MRI has the ability to detect ventilation defects where are absent or have relatively low signal intensity within the lung [2, 3]. Dissolved-phase MRI can measure gas uptake by lung parenchyma and blood flow [4]. Progress in deep learning makes it possible to quantify ventilation defect percentage and gas uptake ratios among different lung lobes, providing valuable information for regional analysis of these measurements [5].

However, current HPG imaging lacks standardization, making it difficult to interpret study results among different subjects and institutions. In this study, we investigated the ventilation defect percentage (VDP) of 50 healthy subjects diversified race, gender, age, BMI and smoking history. Our findings would serve as a reference for the VDP in health subjects. For dissolved-phase MRI, we found the

lung volume during MRI scan influences the resulting gas uptake ratios. We investigated a total of 17 subjects including 11 healthy subjects and 5 COPD patients who underwent dissolved-phase MRI in three different lung inflation levels. We got strong inverse correlations between lung inflation level and gas uptake measurements obtained by hyperpolarized Xe-129 MRI. Regional distribution of gas uptake and the influence of different inflation levels on each lobe were further investigated. These results would benefit the standardization and popularity of hyperpolarized Xe-129 MRI in the application of assessing lung function.

To my parents.

Acknowledgements

I would like to thank all the people helping me make this thesis research possible, and anyone giving me instruction and support during my master's study at the University of Virginia.

To begin with, I would like to give my sincere appreciate to my advisor, Dr. Kun Qing, who guided me during my entire time at UVa. He helped me a lot not only in research, but also in study and life. With his help, I was able to quickly adapt to the environment in the United States, and realize my study and research goals step by step. He was always patient with every question I had, offered me resources I might need, and showed me how to conduct scientific research studies. I would also like to thank my graduate committee chair, Dr. Craig Meyer, for his instructions in the Biomedical Measurement Principles course and the efforts he made on advising my thesis. I benefited a lot from his abundant knowledge in MRI and attitude toward research. I also learned a lot from another committee member, Dr. Y. Michael Shim. He always offered me the insights in lung physiology, and led me understanding the results physiologically. He also instructed me a lot in seeking appropriate approach for analyzing data.

I would like to greatly thank Dr. Nick Tustison, Dr. John Mugler, III and Dr. Jaime Mata in our HPG imaging team. Dr. Tustison mentored me in the deep learning part in my research. His expertise in medical image processing and deep learning gave me a chance to improve myself in computer science field. I also obtained substantial help from Dr. Mugler. Each time I met problems, I always found answers from him, whether in MRI or pulmonary physiology aspects. Dr. Mata also gave me a lot of help and support during my research in medical imaging.

I would like to thank Dr. Xue Feng. With his patient instruction, I gradually learn how to develop software and how to deploy our research on web application to benefit users. I would also like to thank Dr. Ching Yee Tan and Dr. Lukasz Myc,

who worked together with me in projects on healthy and COPD subjects. We often discussed on the data and approaches, which gave me lots of inspiration on my thesis. I would also like to thank all my classmates and colleagues ever studying and working with me. I will never forget the wonderful time we spent on each course and project. Those are my cherished memories at UVa.

At last, I would like to give my thanks to my beloved parents and family who stand behind me and support me all the time. The achievements I have attained would not been possible without their constant love.

I apologize I can't mention every person who helped me ever. My single achievement is the result of everybody's efforts.

Table of Contents

List of Tables

List of Figures

Acronyms

FEV_1 forced expiratory volume in one second. xiv, 9, 21, 30, 32–34, 43

ADC apparent diffusion coefficient. 48

ATS American Thoracic Society. 7

BMI Body mass index. iv, 30, 32

CDC Centers for Disease Control and Prevention. 7

CNN Convolutional Neural Network. x, xiii, 23, 25, 28, 29

COPD chronic obstructive pulmonary disease. v, viii, xi, xii, xiv, xv, 7–11, 17–20, 23, 37, 38, 42, 43, 45, 48–50, 52, 53, 55–59

CT computed tomography. iv, 12, 13, 17, 18

DLCO diffusing capacity for carbon monoxide. 10, 11, 38, 39

DP dissolved-phase. 44, 47–50

ERV expiratory reserve volume. 4

FRC functional residual capacity. 9, 10

FVC forced vital capacity. xiv, 4, 9, 21, 30, 32–34, 42, 44–46, 48, 52, 54

He helium. 14, 15, 24, 48

HPG hyperpolarized gas. iv, vii, x, xiv, 14, 15, 19, 21, 22, 24, 30, 34, 38

IC inspiratory capacity. 9

IND Investigational New Drug. 23, 42

IRB Institutional Review Board. 24, 42

IRV inspiratory reserve volume. 4

JLF joint label fusion. 28, 29

MRI magnetic resonance imaging. iv, v, vii, x, xiv, 13–16, 18–22, 25, 30, 31, 34, 37, 38, 40–44, 46–48, 50–52, 60

PET positron emission tomography. 14

PFTs pulmonary function tests. ix, 8, 17, 21, 31

RBC red blood cell. 39, 44, 46–50, 53, 54

RV residual volume. 4, 9, 20, 42, 44–46, 48, 49, 52, 54

SNR signal-to-noise ratio. 12, 15, 18

SPECT single photon emission computed tomography. 14, 18

TLC total lung capacity. xiii, xiv, 4, 9, 20, 42, 44–50, 52, 54, 56–59

TV tidal volume. 4

VDP ventilation defect percentage. iv, xiii, xiv, 30–36

Xe xenon. v, x, xiv, 14–16, 19–21, 24, 30, 31, 38–45, 51, 52, 60

Chapter 1

Introduction

1.1 Physiology Background

Respiration is a sequence of events that result in the exchange of oxygen and carbon dioxide between the atmosphere and cells. Every 3 to 5 seconds, nerve impulses stimulate the breathing process, or ventilation and moves air through a series of passages into and out of the lungs. Exchange of gases between the lungs and the blood is called external respiration. The blood transports the gases to and from the tissue cells. Exchange of gases between the blood and tissue cells is called internal respiration. Finally, cells utilize the oxygen for their biologic activities, and this is called cellular metabolism, or cellular respiration. Together, these activities constitute respiration.

1.1.1 Lung Function and Anatomy

Lung is an organ performing gas exchange with atmosphere. During inspiration and expiration, the body brings in oxygen needed for cellular metabolism, and expels carbon dioxide containing metabolic wastes. This cyclic respiration process ensures the continuous supply of oxygen necessary to maintain life.

The lungs are spongy, air-filled organs located on either side of the chest. The right lung is shorter, broader, and has a greater volume than the left lung. Each lung is composed of smaller units called lobes. Fissures separate these lobes from each other. The right lung consists of three lobes: the superior (upper), middle, and inferior (lower) lobes. The left lung consists of two lobes: the superior (upper) and inferior (lower) lobes. A bronchopulmonary segment is a division of a lobe, and each lobe houses multiple bronchopulmonary segments. Each segment receives air from its own tertiary bronchus and is supplied with blood by its own artery. Some diseases of the lungs typically affect one or more bronchopulmonary segments, and in some cases, the diseased segments can be surgically removed with little influence on neighboring segments. The bronchopulmonary segments are further subdivided into lobules as the bronchi branch into bronchioles. Each lobule receives its own large bronchiole that has multiple branches. An interlobular septum is a wall composed of connective tissue, which separates lobules from one another.

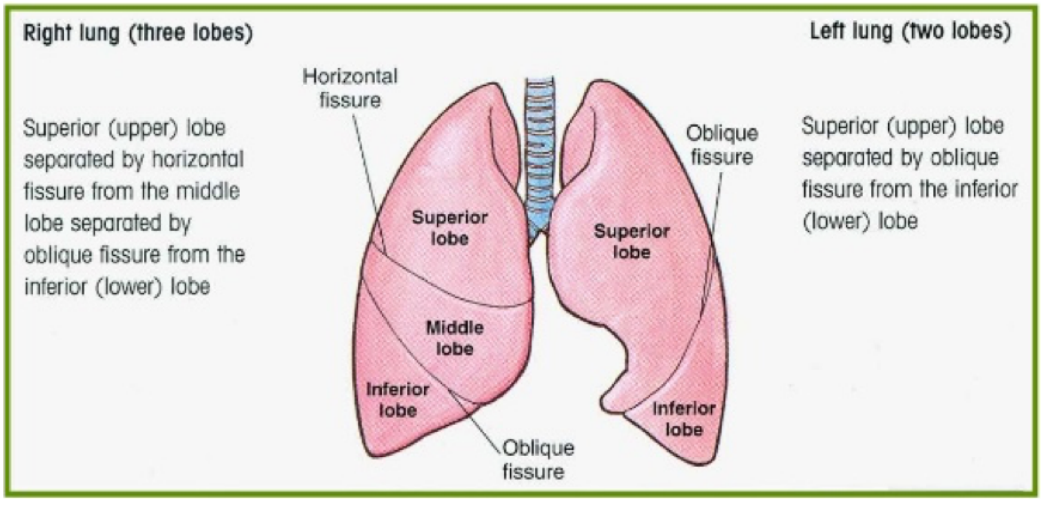

Figure 1.1: Lung anatomy. The right lung (left in the picture) is composed of three lobes: superior (upper), middle and inferior (lower). The left lung has two lobes: superior (upper) and inferior (lower). Lobes are separated by fissures. Reprinted from [6].

1.1.2 Normal Lung Airflow Physiology

Pulmonary ventilation, or breathing, is the movement of air through the conducting passages between the atmosphere and the lungs. The air moves because of pressure gradients between the atmosphere and the negative pressure in the alveoli produced by contraction of the diaphragm and thoracic muscles. Muscular breathing movements and recoil of the elastic tissues (bone and cartilage) create the changes in pressure that result in ventilation.

Lung volumes, or respiratory volumes, refer to the volumes of gas in the lungs at a given time during the respiratory cycle. Lung capacities are sums of two or more lung volumes. The amount of air in the lungs can be subdivided into four standard volumes (tidal, inspiratory reserve, expiratory reserve, and residual) and four capacities (inspiratory, functional residual, vital and total lung capacities). The relationships among the lung volumes and capacities are shown in Figure 1.2 and listed below [7]:

Tidal Volume (TV): the amount of air that can be inhaled and exhaled during one normal (quiet) breathing cycle (about 500 ml for men & women).

Inspiratory Reserve Volume (IRV): the amount of air that can be forcibly and maximally inhaled beyond a tidal inhalation (about 3,000 ml for men & 2,000 ml for women).

Expiratory Reserve Volume (ERV): the amount of air that can be forcibly and maximally exhaled from end-tidal volume to point of maximal exhalation (RV). (about 1200 ml for men & 700 ml for women).

Residual Volume (RV): the amount of air remaining in lungs after maximal exhalation (about 1,200 ml in men & women).

Inspiratory Capacity (IC): maximum inspiration from end-tidal volume to total lung capacity, sum of TV and IRV.

Vital (FRC): volume of air remaining in chest at the end of a tidal volume breath, sum of ERV and RV.

Vital Capacity (VC): maximum volume exhaled after maximum inspiration.

Total Lung Capacity (TLC): volume of air in lungs at end of maximal inspiration, sum of IRV, TV, ERV and RV.

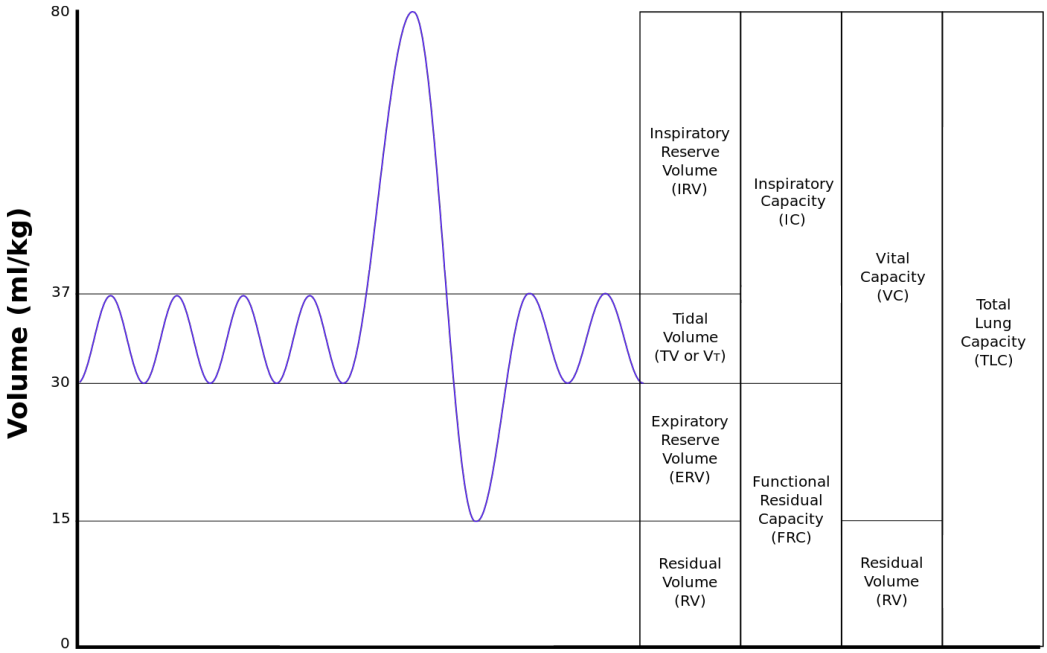

Figure 1.2: Lung volumes and capacities. Reprinted from [8].

Lung volumes are an important aspect of pulmonary function testing because they can provide information about the physical condition of the lungs. Factors such as depth of respiration, ethnicity, age, gender, body composition [9], and physical conditioning influence lung volumes and capacities. A number of the lung volumes can be measured by Spirometry: TV, IRV, and ERV. However, measurements of RV, FVC, and TLC are through body plethysmography, nitrogen washout or helium dilution techniques, which are described in detail in Section 1.2.1.

1.1.3 Normal Lung Gas Exchange Physiology

Gas exchange occurs at two sites in the body: in the lungs, where oxygen is picked up and carbon dioxide is released at the respiratory membrane, and at the tissues, where oxygen is released and carbon dioxide is picked up. The former one is the exchange of gases with the external environment, called external respiration, and the latter one is the exchange of gases with the internal environment, called internal respiration. The actual exchange of gases occurs due to simple diffusion which follows pressure gradients. Energy is not required to move oxygen or carbon dioxide across membranes. The anatomy of the lungs maximizes the diffusion of gases: the respiratory membrane is highly permeable to gases, minimizes the distance of diffusion with very thin respiratory and blood capillary membranes, and maximizes the surface area for gas exchange throughout the lungs.

Pulmonary ventilation transports air to the alveoli for external gas exchange process. The alveoli are surrounded by a mesh of capillaries. Oxygen from the inhaled air passes through the alveolar epithelium and into the blood. The pulmonary artery carries deoxygenated blood into the lungs from the heart, where it branches and eventually becomes the capillary network composed of pulmonary capillaries. These pulmonary capillaries create the respiratory membrane with the alveoli. As the blood is pumped through this capillary network, gas exchange occurs (Figure 1.3). At the respiratory membrane, where the alveolar and capillary walls meet, gases move across the membranes, with oxygen entering the bloodstream and carbon dioxide exiting. Most of the oxygen is picked up by erythrocytes (red blood cells) and oxygenated blood returns to the heart through the pulmonary veins. Carbon dioxide is released in the opposite direction of oxygen, from the blood to the alveoli. It is through this mechanism that blood is oxygenated and carbon dioxide, the waste product of cellular respiration, is removed from the body. After absorbing oxygen, the blood leaves the lungs and is carried to your heart. Your heart then pumps it through your body to

provide oxygen to the cells in organs and tissues. As the cells use the oxygen, carbon dioxide is produced and absorbed into the blood. The blood then carries the carbon dioxide back to your lungs, where it is removed from the body during the exhalation.

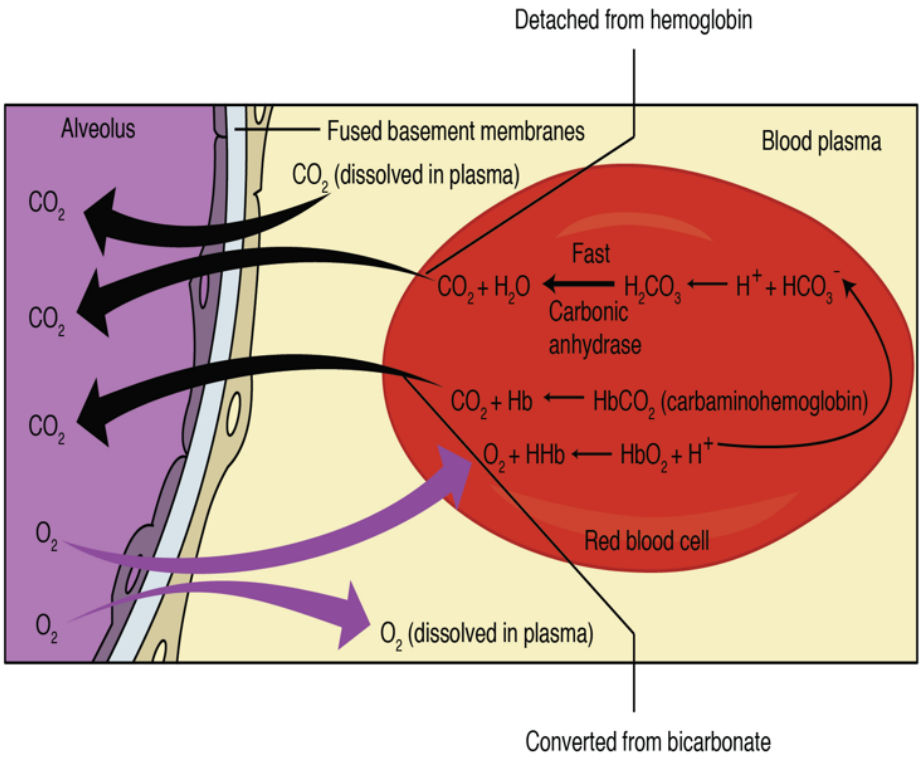

Figure 1.3: Gas exchange between alveolus and red blood cell. Reprinted from [10].

1.1.4 Abnormal Lung Function and Respiratory Diseases

Respiratory disease is an important health issue in the United States. In 2016, chronic lower respiratory diseases (including asthma and chronic obstructive pulmonary disease) were the 4th leading cause of death in the United States, with more than 150 thousand people dying from them, and millions more suffering from them but without being diagnosed [1].

Asthma

Asthma is a chronic inflammatory disorder of the airways characterized by variable and recurring symptoms, airflow obstruction and bronchial hyperresponsiveness [11]. According to statistics and analysis by U.S. Centers for Disease Control and Prevention (CDC), more than 26 million (8.2%, 1 in 13) people in the U.S. have asthma (2016) [1], and it is one of the most common chronic diseases of childhood, affecting an estimated 6 million children [11]. The common symptoms of asthma include cough, wheezing, chest tightness and shortness of breath. These episodes are usually associated with widespread but variable airflow obstruction that is often reversible either spontaneously or with treatment [11]. The causes of asthma involve host factors (particularly genetics) and environmental exposures that occur at a crucial time in the development of the immune system. A definitive cause of the inflammatory process leading to asthma has not yet been established. Methods which help assess airway anatomy, regional lung mechanics and associated lung function (e.g., gas exchange) can promote understanding of the differences between the lungs of healthy subjects versus those with asthma, or of the severity of asthma [12]. Although there are therapeutic approaches for controlling symptoms, reducing airflow limitation and preventing exacerbations [11], various phenotypes of asthma and complex pathology still desire new approach to provide better understanding and treatments of the disease.

Chronic obstructive pulmonary disease (COPD)

As defined by the American Thoracic Society (ATS), chronic obstructive pulmonary disease (COPD) is a preventable and treatable disease state characterized by airflow limitation that is not fully reversible. The airflow limitation is usually progressive and is associated with an abnormal inflammatory response of the lungs to noxious particles or gases, primarily caused by cigarette smoking [13]. According to CDC,

approximated 16 million adults have been reported to be diagnosed with COPD (2013) [14], and millions more suffer from COPD without being diagnosed [15].

COPD comprises pathological changes in four different compartments of the lungs (central airways, peripheral airways, lung parenchyma and pulmonary vasculature), which are variably present in individuals with the disease [16, 17, 18, 19, 20]. The physiological abnormalities in COPD include: mucous hypersecretion and ciliary dysfunction; airflow limitation and hyperinflation; gas exchange abnormalities; pulmonary hypertension; and systemic effects [21, 22]. The diagnosis of COPD usually depends on spirometry as a global assessment of pulmonary physiology.

1.2 Tools for Assessing Lung Physiology

1.2.1 Pulmonary Function Tests (PFTs)

Airflow and lung volume measurements can be used to differentiate obstructive from restrictive pulmonary disorders, to characterize severity, and to measure responses to therapy. Measurements are typically reported as absolute flows and volumes or as percentages of predicted values using data derived from large populations of reference cohorts presumed to have normal lung function. Variables used to predict normal values include age, sex, ethnicity, and height. PFTs are often used in a variety of lung disease diagnosis. PFTs mainly contain spirometry, spirometry before and after a bronchodilator, lung volumes, and quantitation of diffusing capacity for carbon monoxide. Additional PFTs, such as measurement of maximal respiratory pressures, flow-volume loops, submaximal exercise testing, and bronchoprovocation challenge, are useful in specific clinical circumstances.

Spirometry

Spirometry is the most widely used PFT in clinic. It quantifies the airflow moving in and out of the lungs. In the assessments, the volume of air exhaled at specific time points during forceful and complete exhalation after a maximal inhalation is recorded by an instrument called spirometer. The volumes measured include the total exhaled volume, known as the FVC, the volume exhaled in the first second, known as the forced expiratory volume in one second (FEV_1), and their ratio (FEV_1/FVC) [23]. The test takes 10 to 15 minutes and carries minimal risk (e.g., rarely syncope). Performance of spirometry before and after bronchodilator is used to determine the degree of reversibility of airflow limitation.

Spirometry is a key diagnostic test for asthma and COPD (when performed before and after bronchodilator) and is useful to assess for asthma or other causes of airflow obstruction. In patients with asthma, bronchodilator administration often results in improvement, and in some patients with asthma, post-bronchodilator testing may improve to normal spirometry values. Among patients with COPD, administration of bronchodilator sometimes leads to a significant change in FEV_1 but reversal to normal spirometry rules out a diagnosis of COPD [24]. Bronchodilators may also lead to improvement in flow in the small airways and a reduction in air trapping. While criteria for assessment of reduced air trapping have not been formalized, an increase in IC and a decrease in FRC are thought to reflect this response.

Lung Volume Measurements

Respiratory (pulmonary) volumes are important aspect of PFT because they can provide information about the physical condition of the lungs. RV constitutes part of FRC as well as TLC, and simple spirometer is incapable of measuring these parameters. The procedures used for measurement of RV, FVC and TLC are based on radiological, plethysmographic or dilutional techniques [25].

Gas dilutional techniques include helium dilution and nitrogen washout methods. With nitrogen washout, the patient exhales to FRC and then breathes from a spirometer containing 100% oxygen. The test ends when the exhaled nitrogen concentration is zero. The collected volume of exhaled nitrogen is equal to 81% of the initial FRC. With helium equilibration, the patient exhales to FRC and then is connected to a closed system containing known volumes of helium and oxygen. Helium concentration is measured until it is the same on inhalation and exhalation, indicating it has equilibrated with the volume of gas in the lung, which can then be estimated from the change in helium concentration that has occurred.

Both of these techniques may underestimate FRC because they measure only the lung volume that communicates with the airways. In patients with severe airflow limitation, such as moderate to severe COPD patients, a considerable volume of trapped gas may communicate very poorly or not at all, because they do not access under or nonventilated areas.

Body plethysmography is the gold standard for measurement of lung volumes. It's more accurate than dilution techniques in patients who have significant airflow obstruction [26]. Body plethysmography uses Boyle's law ($P_1V_1 = P_2V_2$) to measure the compressible gas volume within the thorax. While sitting in an airtight box, the patient tries to inhale against a closed mouthpiece from FRC. As the chest wall expands, the pressure in the closed box rises. Knowing the pre-inspiratory box volume and the pressure in the box before and after the inspiratory effort allows for calculation of the change in box volume, which must equal the change in lung volume.

Diffusing capacity of carbon monoxide (DLCO)

Single-breath diffusing capacity for carbon monoxide (DLCO), also known as transfer factor of carbon monoxide (TLCO), measures the quantity of carbon monoxide transferred from alveolar gas to red blood cells in pulmonary capillaries per minute.

Measuring DLCO is a quick, safe and useful way to evaluate restrictive and obstructive lung diseases, as well as pulmonary vascular disease. In the setting of restrictive lung diseases, DLCO helps to distinguish between interstitial lung diseases, in which DLCO is usually reduced, and other causes of restriction, in which DLCO is usually normal []. In obstructive disease, the DLCO helps to distinguish between emphysema and other causes of chronic airway obstruction. The DLCO is also used in the assessment of pulmonary vascular disease (e.g., thromboembolic disease, pulmonary hypertension), which typically causes a reduction in DLCO in the absence of significant restriction or obstruction.

1.2.2 Clinical Imaging

There is growing need to evaluate newly developed therapies and to better understand the underlying mechanisms leading to development of pulmonary diseases. Imaging techniques that can provide regional information on the structure and function of the lung are highly desirable to help address this need.

Chest X-ray

The chest radiograph, or chest X-ray, is the oldest and the most frequently used radiological procedure in lung disease screening and diagnosis. As it provides structural information in and around the thorax, and it is often the first step in the radiological evaluation of patients with suspected respiratory diseases. Specifically, chest X-ray provides general testing as an initial diagnostic study and is especially useful in the diagnosis of pneumonia, cancer, and COPD. Fluoroscopy (an X-ray technique by which respiratory movement is visualized directly) is used mainly for guidance of biopsy of peripheral lung lesions and for differential diagnosis of an elevated diaphragm. Modern radiography offers high image quality and lower radiation dose, making it is still the standard technique for initial investigations, especially in cases of infectious, ma-

lignant, or obstructive airway disease [27]. However, conventional chest X-ray is of limited use since pulmonary lobules cannot be visualized with plain film radiography.

Chest computed tomography (CT) scan

Chest CT is a standard procedure in diagnosing many lung diseases [28]. Compared to chest X-ray, CT has higher spatial resolution and signal-to-noise ratio in assessing lung parenchyma and surrounding structures [29]. Chest CT is highly recommended if there is doubt of the diagnosis and in preparation for bullectomy or lung volume-reduction surgery, determine the extent of cancer, and detect presence of interstitial lung diseases. Progress in multidetector CT (MDCT) makes it possible to obtain high and isotropic resolution images at the same radiation exposure in a 10-second breath-hold, allowing the image dataset to be viewed in any plane desired [29, 30].

Specific CT techniques can be applied in varied lung disease diagnosis. Low-dose CT is used in follow-up and serial early lung cancer detection [31]. High-resolution CT (HRCT) techniques improve the diagnosis of interstitial lung disease, emphysema and bronchiolitis considerably [29] by allowing direct measurements of airway wall thickness in the same patients at the same time with inspiratory and expiratory breath-hold maneuver [32, 33]. Besides assessment of morphological changes in the lung parenchyma, CT can be used to gain functional information – perfusion, with the inherent high spatial resolution [34]. The newest MDCT scanners are equipped with dual- energy technology, meaning that two different energies/tube voltages are used at the same time. Because of the energy dependence of absorption, particular tissue characteristics can be emphasized, e.g., iodine distribution after contrast administration as a surrogate for regional perfusion [35].

Proton magnetic resonance imaging (MRI)

Because of the absence of ionizing radiation, magnetic resonance imaging (MRI) is a promising alternative to the CT in providing structural and functional information of the body. MRI employs magnetic resonance of hydrogen protons to generate images containing structural and functional information. As body content is mainly fluid (H_2O), MRI provides unique contrast between tissues with varying degrees of fluid content.

Proton MRI is useful in assessment of superior sulcus tumors, possible cysts, and other lesions that abut the mediastinum and chest wall. Because of the excellent visualization of vascular structures, proton MRI has a role in the diagnostic investigation of vascular diseases such as pulmonary hypertension, or complex diseases such as cystic fibrosis [28].

However, proton MRI has inherent shortcomings in pulmonary imaging, as there is very low abundance of fat and water, corresponding to weak H-1 signal. To make up this shortcomings, hyperpolarized gases used as contrast agents can be employed to image the lung with MRI, which will be talked in detail in Section 1.3.2.

1.3 New Techniques

1.3.1 Molecular Imaging

Continued progression of treatment options for chronic pulmonary diseases has led to the increasing need to develop molecular imaging tools for diagnosis, treatment planning, drug discovery and therapy monitoring [36]. Molecular imaging has its advantages over current clinical tools as it has the ability to detect the alternations of molecular activities underlying diseases. This specific subcellular level detection allows earlier and more accurate diagnosis than detecting overall late morphologic

manifestations. It also permits the detection of drug or treatment responses to be much earlier. Positron emission tomography (PET) and single photon emission computed tomography (SPECT) are the most common imaging modalities for molecular imaging.

Lung inflammation, infection, pulmonary physiology and lung malignancies are major pulmonary disorders that can be investigated by molecular imaging. In the early phases of inflammation, there may be not obvious morphologic alternations that can be detected by conventional imaging techniques. Molecular imaging, however, can potentially detect these abnormal events, the infectious agent itself and also the increased metabolic activity. Molecular imaging approaches may also facilitate the translation of effective targeted therapies for lung disease. The identification and validation of lung-specific biomarkers that can assess the response to a particular targeted pathway during a therapeutic intervention could dramatically increase the efficiency of drug development.

1.3.2 Hyperpolarized Gas (HPG) Magnetic Resonance Imaging (MRI)

As we talked in Section 1.2.2, proton MRI has limitations in pulmonary imaging as low water content in lung. Using hyperpolarized noble gases helium-3 (He-3) or xenon-129 (Xe-129) as inhaled contrast agents makes up this shortcoming of proton MRI for evaluating airways and airspaces.

In proton MRI, the spin polarization which is used for imaging is determined by the Boltzmann equilibrium. However, the concentration of inhaled noble gas in vivo is small to allow MR imaging. To overcome this obstacle, the nuclear moments of He-3 and Xe-129 can be hyperpolarized five magnitudes above the Boltzmann equilibrium through transfer of angular momentum using optical pumping, compensating for their 1000 times lower densities in vivo compared with liquid state hydrogen concentrations

in tissue [37]. By having a large nuclear polarization, they can be easily detected with an MR scanner tuned to the appropriate resonant frequency [38]. Moreover, recent advancements in gas polarization technologies improve Xe-129 production rates with order-of-magnitude, to liter per hour at 50% polarization [39], allowing clinical lung imaging with hyperpolarized Xe-129 to be more feasible [39, 40].

The applications of He-3 have been well demonstrated. However, He-3 has extremely low solubility in blood, and it is not widely used due to its limited supply and rising price [41, 42, 43, 44, 45]. For these reasons, Xe-129 has become an attractive alternative as its unlimited supply in the atmosphere and relatively low cost. Moreover, it is extraordinarily sensitive to its chemical environment, which results in large range of chemical shifts upon solution [46]. These characteristics of Xe-129 make it possible to explore certain lung structures and function, such as pulmonary airspaces, lung microstructure, regional ventilation, perfusion and alveolar gas uptake. Hyperpolarized gas imaging overcomes the SNR challenge faced in proton MRI and allows for the direct imaging of lung airspaces.

1.4 Thesis Overview

This thesis is organized as follows.

Chapter 2 describes the rationale of this thesis. It explains the limitation of current clinical tools in assessing lung function, and the advantage of HPG MRI over them in regional and quantitative analysis. It also points out the lack of standardization of current HPG MRI techniques. The rest work of this thesis will address this need.

Chapter 3 describes the application of hyperpolarized Xe-129 MRI in quantifying ventilation defects. Specifically, a basic explanation of the HPG ventilation MRI, as well as the quantification method realized by deep learning, is provided. Our work in analyzing ventilation defects in healthy subjects is also described in this chapter.

Chapter 4 describes the application of Xe-129 MRI in assessing gas uptake by lung tissue and red blood cells. The basics of dissolved-phase MRI is explained here. This chapter also pointed out the current issue of dissolved-phase MRI – the variation in protocols, and proposed lung volume as an important parameter in dissolved-phase imaging.

Chapter 5 describes the study in analyzing the relationships between lung inflation level and gas uptake measures acquired by corresponding MRI acquisitions.

Chapter 6 describes the lobar analysis of gas uptake ratios. The effects of lung inflation level on lobar dissolved-phase MRI results are also discussed here.

Chapter 7 summaries the work in this thesis and discusses the possibilities of future developments.

Chapter 2

Rationale

2.1 Limitation of Conventional Modalities

Common techniques to diagnose asthma and COPD include medical history, physical examination, PFTs, chest radiography and X-ray CT. Since there is growing need for improved tools for applications like monitoring the lung functional response to new treatments or aiding in the rapid development of novel respiratory drugs targeting COPD, tools for regional quantification of lung function are needed.

Currently available tools are not sensitive to early detection and provide little information as to the regional distribution of diseases. The shortcoming of PFTs is reflected in the recent 2017 GOLD group classification system: escalation of medical therapy in the longitudinal management of COPD is now exclusively based upon the functional status of the patient and their exacerbation frequency, rather than the spirometry-based classification system in the past.

Chest X-ray CT has emerged as the choice for comprehensive assessment of the lung by providing a detailed assessment of the airway and vascular trees, parenchyma, pulmonary blood volume [47], and regional ventilation [48]. However, it is still limited in assessing lung function. With the current limits of CT resolution, the small

airways are not well resolved [29]. Moreover, current CT techniques are not very sensitive to the early changes of the lung during initial stages of COPD, and are not sensitive enough to monitor gradual disease progression. Although CT allows assessment of pulmonary function by obtaining images with inhalation of xenon gas and determining the wash-in and wash-out rates, the image resolution and repeatability of these techniques under current technical conditions are limited. Concern about ionizing radiation further hinders its feasibility, as well as that of techniques such as single photon emission computed tomography (SPECT), particularly when repeated imaging is needed longitudinally or the target subjects are children.

Clinical proton MRI of the lung is also under challenges. The inherently low water and fat density and short T2* in lung tissues compared to other tissues in the human body result in images with a poor quality [49, 50]. Furthermore, the multitude of air-tissue interfaces within the lung also create significant magnetic field distortions, commonly described as susceptibility artifacts, which further diminish the lung MR H-1 signal. Additionally, respiratory and cardiac motion during image acquisition degrades pulmonary MR image quality [29]. Although there has been progress in proton MRI of the lungs using ultra-short echo time sequences to increase signal-to-noise ratio (SNR) [51, 52], proton MRI still has shortcomings in evaluating pulmonary structure and function. For example, it cannot directly image the airspaces, and is limited in exploring the physiological function of the lungs.

In summary, it remains challenging to obtain *in vivo* regional depiction and quantification of the most basic physiological functions of the lung – gas delivery to the airspaces and gas uptake by the lung parenchyma and blood – in a manner suitable for routine application in humans.

2.2 Advantages of Hyperpolarized Xe-129 MRI Compared to Conventional Modalities

Hyperpolarized Xe-129 MRI has some advantages over conventional modalities in several aspects. *First*, MRI is a technique that doesnt expose subjects to radiation, allowing it to be repeated multiple times in a single day if desired. *Second*, MR images could provide regional information of the lung. The regional ventilation and gas uptake-exchange throughout the lungs can be assessed to gain a better understanding of pulmonary physiology and disease progression [53]. For example, HPG MRI is useful in identifying ventilation-perfusion mismatch in patients with pulmonary embolism, in staging and tracking the success of therapeutic approaches in patients with chronic obstructive airway diseases, and in identifying candidates for lung transplantation or reduction surgery [54].

2.3 Current Shortcomings of HPG MRI

Although Xe-129 MRI provides valuable information in assessing lung function, it still has several limitations, such as the lack of standardization. Because each institution has its own protocol and workflow, there is not a unified protocol for imaging [55, 4, 56]. Therefore, the results obtained from one institution may not be interpreted in the same way in another institution. In this study, we are trying to build unified reference within healthy and COPD patients, making it possible for HPG MRI to be more widely applied.

Chapter 3

Normal Lung Airflow Physiology Assessed by Hyperpolarized Xe-129 Ventilation MRI

3.1 Introduction

Through ventilation, oxygen is brought into the lungs from the atmosphere and carbon dioxide carried into the lungs in the mixed venous blood is expelled from the body. Regional ventilation abnormalities, such as airway narrowing, air trapping and airway inflammation are associated with airway diseases. As mentioned in Section 1.1.4, obstructive respiratory disorders (e.g. asthma, COPD) are characterized by a reduction in airflow [57, 58]. With decreased airflow, expiration time may become longer than usual, and lung volumes such as TLC and RV may also increase due to air trapping [59]. In patients with asthma and COPD, it may help the clinical decisions to monitor the evolution of these defects as the diseases progress over time during clinical, longitudinal studies.

Not only patients with respiratory disorders, people with normal lung function also show variations in ventilation patterns [60]. Thus, a good starting point is to establish normal lung reference about ventilation. This becomes the main goal of this part of our work.

3.2 Normal Lung References with Spirometry

Normal lung references with spirometry was well illustrated in third National Health and Nutrition Examination Survey (NHANES III) [61]. This study developed spirometric reference values based on 7,429 asymptomatic, lifelong non-smoking participants. Factors including race, height, age and gender were considered. It showed that Caucasians had higher FVC and FEV_1 values than Mexican- and African-Americans had across the entire age range, but these values of Caucasians and Mexican-Americans were similar with respect to height between Caucasians and Mexican-Americans, whereas African-Americans had lower values. These results may partially due to the differences in body build: observed Caucasian subjects were taller than Mexican-Americans of the same age, and had larger trunk-to-leg ratio than African-American subjects had. These reference values have provided extensive benefit in clinical diagnosis as well as in research utilizing PFTs as a diagnostic tool.

3.3 The Assessment of Airflow Physiology Using Hyperpolarized Xe-129 MRI

3.3.1 HPG Ventilation MRI

Spirometry is the primary method to detect abnormal ventilation and establish obstructive lung diseases. However, obstructive diseases often show inhomogeneous ventilation distribution which cannot be detected by spirometry [3], especially in

early pathogenesis involving small airways [62, 63]. The advancements in HPG MRI enable better understanding of lung airflow physiology by visualizing subtle changes in ventilation [12]. Ventilation detected by HPG MRI has shown consistency with spirometry results in both healthy and diseased subjects [64, 12, 65].

HPG MRI can detect areas of abnormal ventilation in the lungs with excellent sensitivity and regional specificity. In general, static ventilation imaging is performed during a single breath-hold after inhaling gas mixture containing a known volume of hyperpolarized noble gas [66]. In ventilation images, normal functional parts of the lung show high signal, while ventilation defects – regions where airflow is partially or totally obstructed, are absent of or have relatively low signal [2, 3], as shown in Figure 3.1.

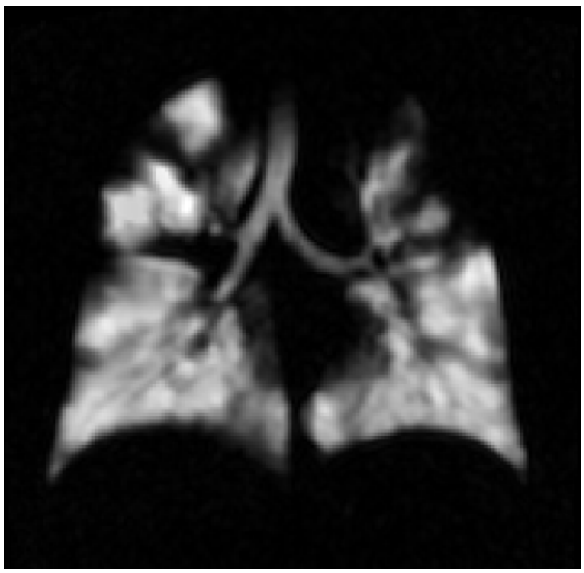

Figure 3.1: HPG ventilation MR image. Normal functional regions are showed high signal, while ventilation defects are absent of signal or shown relatively low signal.

Studies have shown HPG MRI is able to detect ventilation changes in the lung with high sensitivity [67, 64]. For instance, ventilation imaging showed the capability to detect regional airway closure in moderate to severe asthma [64], and changes

before/after breathing albuterol [68]. It also showed sensitivity and regional specificity for detecting obstructive lung diseases like COPD [69].

3.3.2 Quantification of Ventilation Defects Using Convolutional Neural Network (CNN)

Rational and Objectives

With the need of quantitatively analyzing lung ventilation function, computational techniques for the segmentation of MR images are desired. However, previous reported methodologies for identifying proton lung masks and quantifying ventilation defects, including [70, 71], usually require huge time and computational resources. Recent development in machine learning, specifically deep learning [72], gives a possibility to analyze images with high accuracy and time efficiency. By developing and training multiple layers of neural networks, deep learning is able to perform computer vision tasks such as image classification and voxel-wised segmentation. In this work, we developed convolutional neural networks to segment lung masks and quantify ventilation defects [5].

Large data requirement is a key obstacle when training deep learning models [73]. In this work, we deployed a template-based data augmentation strategy [5]. Different from common randomized simulated linear (e.g., translation, rotation and affine), elastic transformations and intensity adjustments (e.g., brightness and contrast), our strategy is shape-based and addresses the characteristics of medical images [5]. Accuracy and time-efficiency are expected by applying this CNN framework.

Materials and Methods

Image acquisition The studies were conducted under U.S. Food and Drug Administration Investigational New Drug (IND) Application for MR imaging with hyper-

polarized gas, and the study protocols were approved by the University of Virginia's Institutional Review Board (IRB). All human subjects signed informed consent after being explained the details of study procedure prior to the studies. HPG ventilation images were composed of both He-3 and Xe-129 acquisitions. MR acquisitions were performed using a 1.5T whole-body MR scanner (Siemens Avanto, Siemens Medical Solutions, Malvern, PA). Hyperpolarized gas chest radiofrequency coils (Rapid Biomedical, Rimpar, Germany; IGC Medical Advances, Mil- waukee, WI; or Clinical MR Solutions, Brookfield, WI) were also used. This study included two imaging protocols to acquire images, both of which combined a gas imaging (both He-3 or Xe-129) and a proton imaging in the same breath-hold. One protocol used a 3-D balanced steady-state free-precession or spoiled gradient echo pulse sequences with isotropic resolution = 3.9 mm, TR = 1.75–1.85 ms, TE = 0.78–0.82 ms, flip angle = 9–10°, bandwidth per pixel =1050–1100 Hz/Pixel, total duration = 10–20 s. The other protocol used a contiguous, coronal, 2-D gradient echo pulse sequence with interleaved spiral sampling scheme, in-plane resolution = 24 mm, slice thick- ness = 15 mm, TR = 8–8.5 ms, TE = 0.8–1.0 ms, flip angle=20° interleaves=12–20 (plus 2 for field map), total duration = 3–8 s.

Overall workflow Our proposed workflow is illustrated in Figure 3.2. We developed one proton U-net model and one ventilation U-net model for proton lung mask segmentation and ventilation-based quantification respectively [5]. The input images of both models were preprocessed using N4 bias correction and denoising algorithm [74]. The predicted lung masks from the proton U-net model were used as an input channel for the ventilation model. Proton masks helped identify region of interest for functional quantification [71, 75, 76].

Training both models were offline before individual subject processing. Data augmentation was performed during each model training. The offline training was computationally intensive but was only performed once.

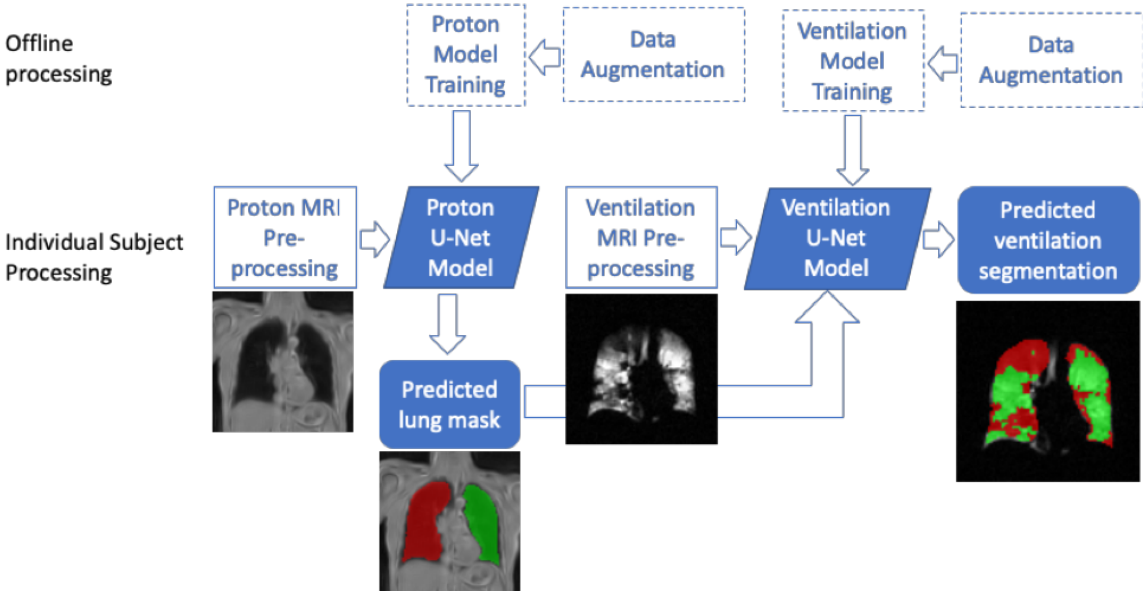

Figure 3.2: Overall workflow of proton MRI segmentation and ventilation-based quantification [5].

CNN Architecture Both our proton and ventilation CNN models were developed based on U-net architecture [77]. U-net has symmetric encoding and decoding paths that linked together via skip paths for enhanced feature detection. Both paths are fully convolutional neural networks [78] and each series is composed of two convolutional layers. We modified the original U-net architecture by adding a dropout layer between two convolutional layers in each series to avoid overfitting. There's also a max pooling layer between each series to produce feature map for the next layer.

Template-based data augmentation To build an effective neural network, large training data is usually a prerequisite [73]. Unlike computer vision area with access to large open-source datasets for training, such as the well-known ImageNet [79], similar

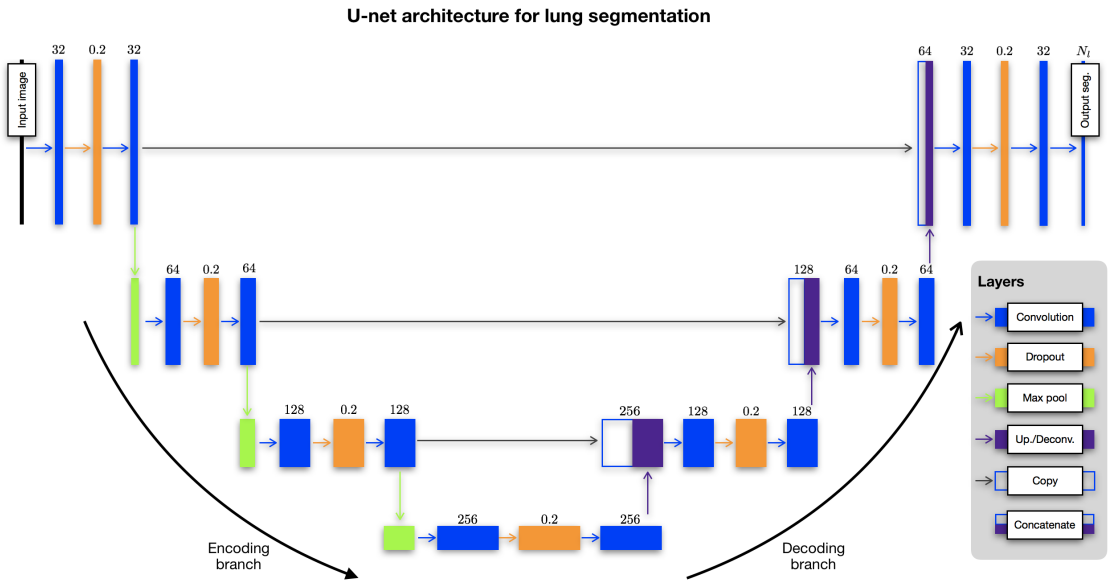

Figure 3.3: The modified U-net architecture for proton lung segmentation and ventilation-based quantification. Network layers are represented as boxes in different colors. Main parameter values are marked above each layer box. Reprinted from [5].

dataset in medical imaging is not easily available. Moreover, common geometric-based (e.g., translation, rotation, affine) and intensity-based (e.g., brightening, contrast) data augmentation methods are not able to address the shape variation information in medical images.

In this work, we proposed a template-based data augmentation strategy to expand the training set [5]. We generated a representative template averaging in shape and intensity from sampled MR images [80]. Transformations to & from each individual image were also generated. This allows each image mapping to the space of another image in the training set. Specifically, for an individual subject S_k, the template-building process generates a transformation to the template φ_k, and an inverse transformation from the template φ_k^{-1}. During the model training, a new image S_{new} can be created by randomly selecting a source image and a target image, and doing the mapping

$$S_{new} = S_{source}(\varphi_{target}^{-1}(\varphi_{source}))$$

By performing this data augmentation, a size of N dataset is possible to be expanded to the size of N^2.

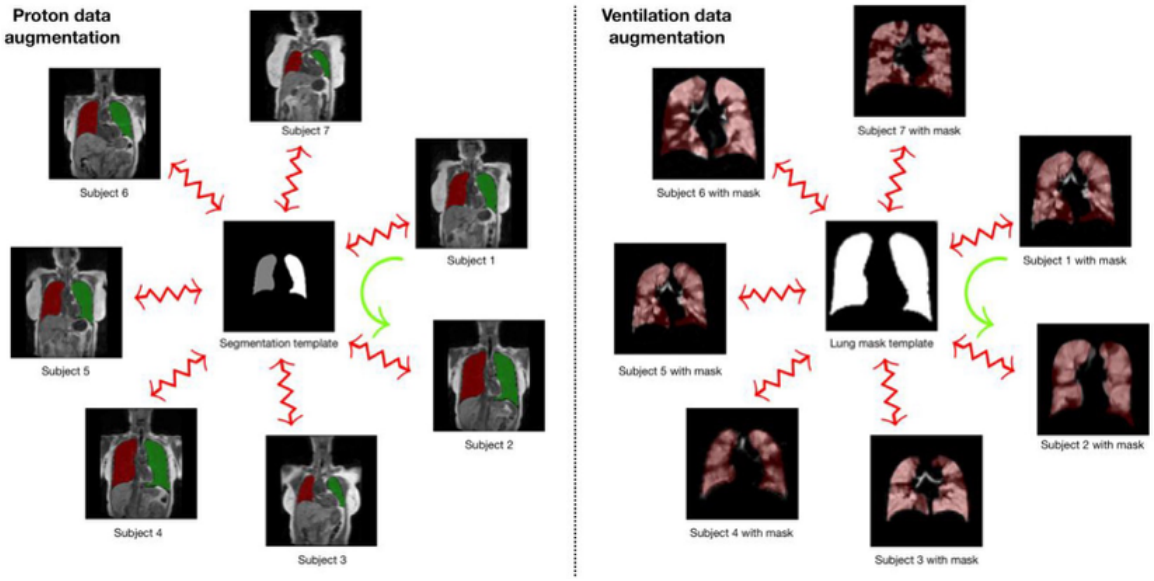

Figure 3.4: Illustration of template-based data augmentation for proton (left) and ventilation (right) U-net model training. Reprinted from [5].

Processing specifics 205 proton images and 73 ventilation images were included in the model training sets. The smaller ventilation dataset was used to ensure class balance. The U-net model for proton image segmentation was 3-D in order to take advantage of the 3-D shape of the lungs. The ventilation U-net model was 2-D, as ventilation images lack sophisticated 3-D shape, and 2-D model takes much less training and predicting time than 3-D while has comparable performance [81]. More practically, the second ventilation acquisition protocol has lower through-plane resolution where 2-D model is more capable with both protocols.

The image size across subjects was not identical, so we resampled proton images to the size of 128 x 128 x 64, and ventilation images to the size of 128 x 128. During proton data augmentation, a "coin flip" was used to randomly vary the intensity

profile of the warped proton images between their original profiles and the intensity profile of the randomly selected reference image [5]. The parameters for CNN models are listed in Table 3.1

Table 3.1: Parameters for CNN models [5].

Adam optimization	
proton model learning rate	0.00001
ventilation model learning rate	0.0001
Number of epochs	150
Training/validation data split	80/20
Convolution layers	
kernel size	5 x 5(x 5)
activation	rectified linear units (ReLU) [82]
number of filters	doubled at every layer starting with N = 16 (proton) and N = 32 (ventilation)
Dropout layers	
rate	0.2
Max polling layers	
size	2 x 2(x 2)
stride length	2 x 2(x 2)
Upsampling/transposed convolution (i.e., deconvolution) layers	
kernel size	5 x 5(x 5)
stride length	2 x 2(x 2)
activation	rectified linear units (ReLU) [82]

Results Evaluation of proton lung segmentation were performed on 62 proton images. We compared the CNN results with a modified joint label fusion (JLF)-based method [70]. The accuracy in terms of Dice overlap for both methods are shown in Table 3.2. Although the accuracy of CNN is slightly lower than JLF, its processing time is significantly shorter: less than 1 second compared to JLF's 25 minutes per subject.

40 ventilation images were tested to evaluate the ventilation model performance. We compared the CNN performance with Atropos software [71] and manual segmen-

Table 3.2: Proton lung segmentation accuracy (in terms of Dice overlap).

	Left Lung	**Right Lung**	**Whole Lung**
CNN	0.93 ± 0.03	0.94 ± 0.02	0.94 ± 0.02
JLF	0.95 ± 0.02	0.96 ± 0.01	0.96 ± 0.01

tation. Because of the absence of ground truth, the STAPLE algorithm [83] was used to create a consensus labeling. The Dice overlap coefficients of three methods are shown in Table 3.3. The processing time for U-net model was less than 1 second per subject, while Atropos was slightly less than 1 minutes, and human readers were 30–45 minutes.

Table 3.3: Ventilation-based quantification accuracy.

	Total	**Normal Lung**	**Ventilation Defect Regions**
CNN	0.94 ± 0.03	0.96 ± 0.03	0.70 ± 0.3
Atropos	0.92 ± 0.03	0.94 ± 0.03	0.71 ± 0.3
Expert reader 1	0.89 ± 0.07	0.91 ± 0.06	0.60 ± 0.3
Expert reader 2	0.92 ± 0.05	0.94 ± 0.04	0.57 ± 0.3
Expert reader 3	0.94 ± 0.03	0.96 ± 0.03	0.63 ± 0.3

Conclusion and Discussion The proposed framework yields comparable accuracy with previously reported methods as well as human readers. Meanwhile, the computational time was significantly shorter than any other methods. This framework permits to enhance analyses of large meta data set which may be commonly present in clinical settings.

There are also several limitations of this framework. The U-net model for ventilation-based quantification was 2-D and therefore the predictions were limited to the coronal view which we were used. 3-D model may achieve better performance from this point. Additionally, other evaluations using clinical measures may be helpful in assessing lung function.

3.3.3 Airflow Physiology in Healthy Subjects Assessed by Hyperpolarized Xe-129 MRI

Rational and objectives

Patients with obstructive diseases often show inhomogeneous ventilation, while the ventilation of people with normal lung function is generally regarded to be homogeneous throughout the lungs [3]. Abnormal ventilation can be detected by spirometry in clinic, but the distribution information of ventilation is absent. Recent advancements in HPG MRI has enabled better detection of small airway physiology and ventilation patterns [12]. It is able to provide quantitative and regional information of ventilation patterns by computing ventilation defect volume to total lung volume ratio, known as ventilation defect percentage (VDP) [84], among different regions of the lungs.

Ventilation defects also emerge in normal lungs [85]. It's known that the normal ranges of spirometry are decreased with age and height. Determining the ventilation patterns of subjects whose spirometry is normal is an essential step to standardize the results obtained by using HPG MRI. This work is to establish a reference of normal lungs with hyperpolarized Xe-129 ventilation MRI.

Materials and Methods

50 healthy subjects within normal spirometry ranges (FEV_1/FVC > 0.7, FEV_1%Pred $> 80\%$, FVC%Pred $> 80\%$) and without any chronic respiratory conditions were included in this study. Demographics and spirometry metrics are shown in Table 3.4. 41 of them were never-smokers and 9 were smokers. Since non-smokers and smokers were significantly different in age and BMI, their effects should be excluded when considering smoking history as a factor. Spirometry results between non-smokers and

smokers were not significantly different, indicating spirometry cannot differentiate them.

Table 3.4: Subject demographics.

	Total (n=50)	**Non-smokers (n=41)**	**Smokers (n=9)**	**p-values between non-smokers and smokers**
Age	50	41.1 ± 17.2	59.0 ± 9.4	0.0040
Gender (m/f)	15/35	13/28	2/7	
Asian	3	3	0	
African American	1	1	0	
Caucasian	46	37	9	
Height (inches)	66.1 ± 3.1	66.4 ± 3.1	64.6 ± 3.9	0.0956
BMI (kg/m^2)	25.0 ± 4.3	24.3 ± 3.7	28.3 ± 5.5	0.0321
Smoking (pk-yr)		0	28.9 ± 9.9	
FEV1/FVC	79.8 ± 5.1	80.2 ± 5.3	77.9 ± 2.5	0.3514
FVC %Pred	108.3 ± 13.0	108.8 ± 13.0	105.9 ± 14.7	0.3085
FEV1 %Pred	104.3 ± 13.6	104.6 ± 12.3	102.7 ± 19.6	0.4143
FEF25-75 %Pred	88.7 ± 20.4	87.9 ± 16.4	91.8 ± 35.5	0.7327

Hyperpolarized Xe-129 MRI acquisitions were performed using a 1.5T commercial whole-body MR scanner. VDP was quantified using our previously reported method [71, 5]. Statistical analyses were performed using Prism 6.0 (GraphPad Software). Linear regressions and Pearson correlation coefficients (r) were assessed in exploring relationships between demographic factors and VDP. Lobar analyses were performed using Mann-Whitney test when data was not normally distributed. Two-way ANOVA was used to determine interactions between regional locations and associated VDP. For all comparisons, the level of significance was 5% ($p < 0.05$).

Results

Significantly elevated VDP was found in some healthy subjects with normal PFTs. The VDP distribution in our study is shown in Table 3.5. The majority

of subjects had VDP range between 10%–20%. However, there were two subjects (4%) showed elevated VDP above 40%. This indicates healthy people can also have severe ventilation defects, even though the spirometry indicates normal.

Table 3.5: VDP ranges of healthy subjects included in the study.

VDP Range	**Number of Subjects**	**Percentage**
0–10	4	8%
10–20	26	52%
20–30	11	22%
30–40	7	14%
40–50	2	4%

In healthy subjects, VDP is directly correlated with aging and inverselyRe correlated with FEV_1/FVC. However, VDP is not significantly correlated with gender, height and weight. We conducted linear regressions between global VDP and each demographic/spirometric factor. Significantly correlation between VDP and age was found (r=0.61, $p < 0.05$, Figure 3.5 left), which indicated older people tend to have more ventilation defects. There was also an inverse correlation between VDP and FEV_1/FVC (r=-0.29, $p < 0.05$, Figure 3.5 right), which consisted with the common knowledge that FEV_1/FVC reflects airflow conditions. However, correlations between VDP and gender, height and BMI were not found.

VDP is similar between healthy smokers and age-matched healthy non-smokers, but their ventilation patterns are highly heterogeneous. There was a significantly difference in VDP between non-smokers and smokers (19.43% $\pm$ 11.13% for non-smokers vs 31.99% $\pm$ 10.27% for smokers, $p < 0.05$, Figure 3.6). However, when comparing age-matched non-smokers and smokers, this difference was not existing any more (26.03% $\pm$ 12.14% for non-smokers vs 31.99% $\pm$ 10.27% for smokers, Figure 3.6).

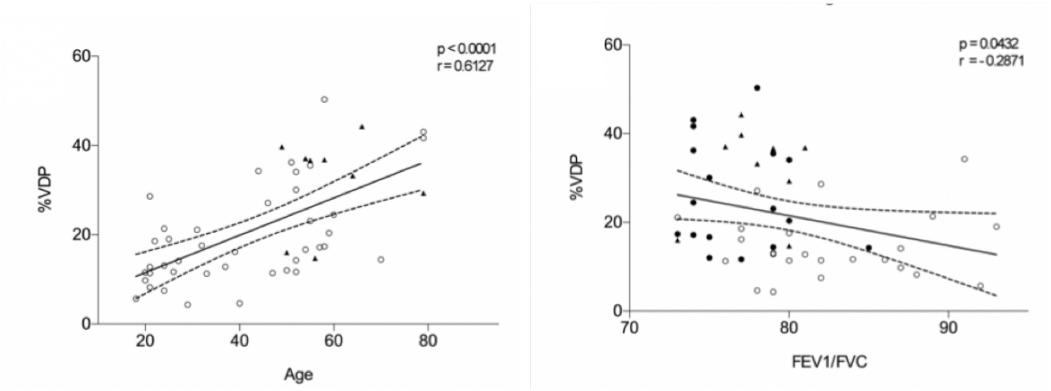

Figure 3.5: Pearson correlations between VDP vs age (left) and FEV_1/FVC (right). Reprinted from [86].

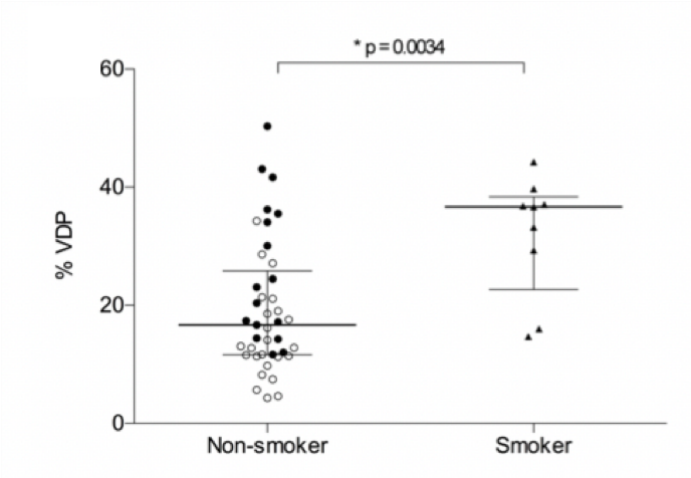

Figure 3.6: VDP of non-smokers and smokers. Open circle represents young non-smoking subjects, closed circle represents older non-smoking subjects age-matched to the smokers, closed triangle represents smoking subjects. Reprinted from [86].

Even though VDP of non-smokers and smokers is similar, they showed very different patterns of ventilation defects. Healthy young subjects showed homogeneous ventilation (Figure 3.7 row 1). Older smokers with low VDP had more heterogeneous patterns of ventilation defects than old non-smokers with similar VDP value (Figure 3.7 row 2&3). Different patterns were also found when comparing older non-smokers and smokers with similar elevated VDP values (Figure 3.7 row 4&5).

Right upper and left upper lobes contribute significantly more to the total VDP. When exploring regional distribution of ventilation among healthy subjects, we found upper lobes (including right upper lobe and left upper lobe) had higher VDP than the other lobes (right middle lobe, right lower lobe and left lower lobe) (9.172%± 5.629% for middle and lower lobes vs $12.52\% \pm 7.893\%$ for upper lobes, Figure 3.8). This suggested upper lobes are more likely to develop abnormal ventilation.

Discussion

Our study showed significant variations in the patterns of ventilation are detectable in "healthy" subjects with normal spirometry. Normal healthy subjects do have a certain degree of abnormal ventilation with unclear clinical significance to one's healthy status. This abnormality can be detected by HPG MRI, demonstrating its superior diagnostic power to spirometry for detecting subclinical abnormalities in human lungs. Through quantitatively analysis, we found VDP by HPG MRI is directly correlated with aging and inversely correlated with subtle drop in FEV_1/FVC. Combining the results with lobar analysis, we conclude that older healthy subjects have disproportionally more significant VDP in upper zones of the lungs.

This work has reflected the ventilation patterns and provided references of healthy subjects at some degree. By continuing collect physiological data from HPG imaging, we believe functional MRI can be more widely applied in assessing lung function.

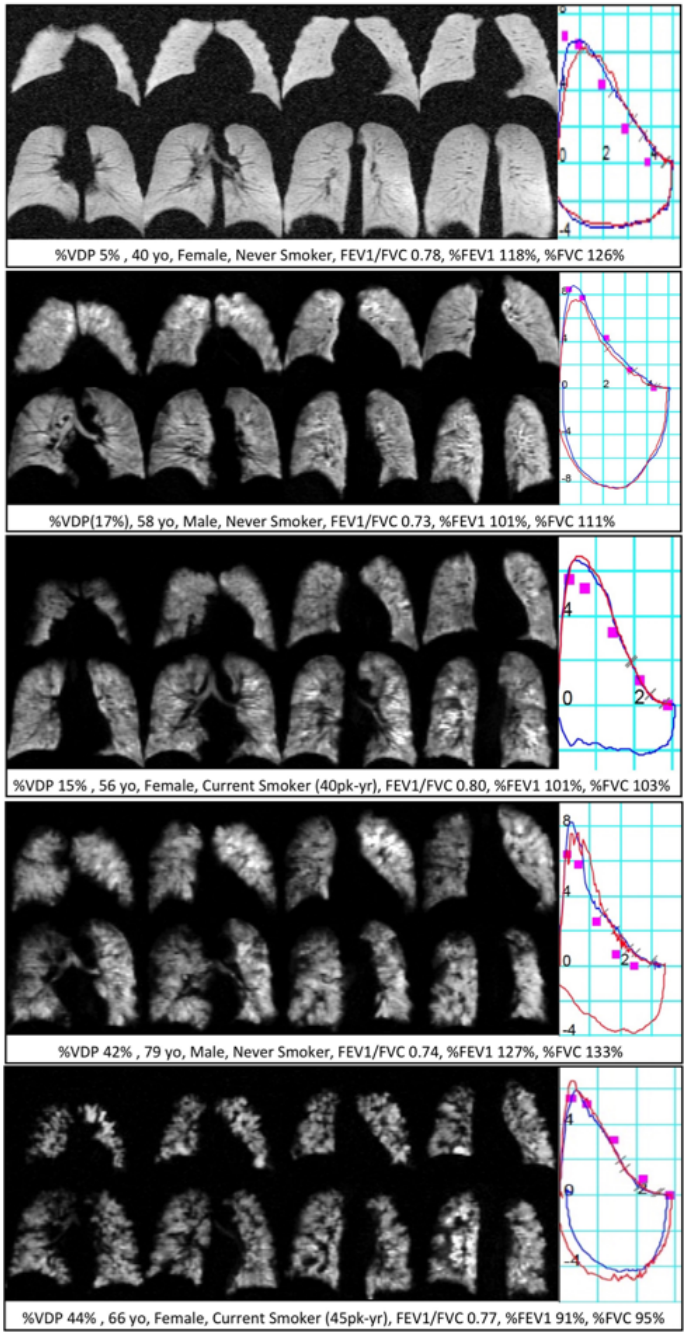

Figure 3.7: Representative ventilation images and flow-volume loops. Row 1: young subject with low VDP, row 2: older non-smoker with low VDP, row 3: older smoker with low VDP, row 4: older non-smoker with high VDP, row 5: older smoker with high VDP. Reprinted from [86].

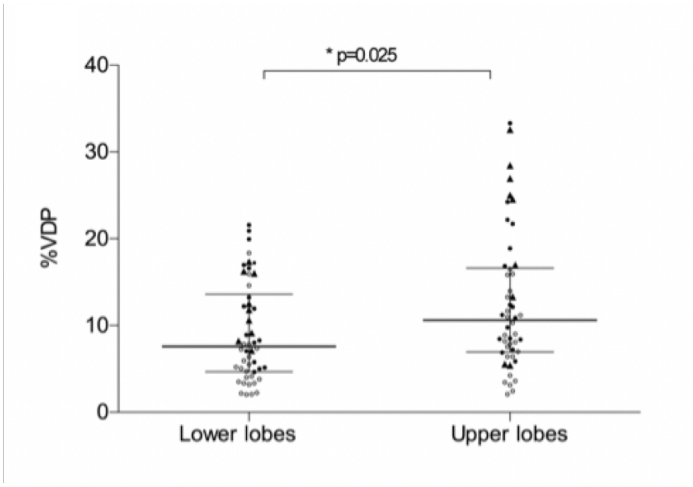

Figure 3.8: VDP of lower lobes (right middle, right lower, left lower) and upper lobes (right upper, left upper). Reprinted from [86].

Chapter 4

Assess gas uptake using dissolved-phase MRI

4.1 Introduction

Gas uptake occurs in external respiration. There are two stages in the uptake of alveolar gases [87] – gas in alveoli diffuses through a semi-solid membrane composed of the alveolar epithelium and capillary walls, and then oxygen in the gas binds to the hemoglobin in the blood flow. The first stage is determined primarily by the thickness and surface area of the membrane, and the second stage depends on the reaction rate with the blood and the capillary blood volume.

Effective pulmonary gas exchange relies on the free diffusion of gases across the thin tissue barrier separating airspace from the capillary red blood cells. Pulmonary pathologies, such as inflammation, fibrosis and edema which cause an increased blood-gas barrier thickness, impair the efficiency of this exchange [88]. Abnormal gas exchange can cause symptomatic shortness of breath, and in severe disease can progress to respiratory failure and death. Patients with lung diseases such as asthma and COPD showed abnormal gas uptake resulted from pathological alterations of lung

tissue or of local blood flow [89, 90]. Thus, effective analysis of lung gas uptake is needed to understanding fundamental process of gas exchange, how heterogeneous diseases such as COPD affect gas exchange, and evaluating new therapeutics for lung diseases [4].

Although our knowledge of gas-exchange status in individual patients is derived primarily from whole-lung measurements, gas exchange can vary substantially within the lung, especially for heterogeneous conditions like COPD and asthma. Thus, quantitative regional assessment of gas uptake would be highly demanded. Although diffusing capacity can be measured by DLCO or stereological methods, DLCO can only provide information of gas exchange, whereas stereological methods cannot yield information in vivo [91]. HPG MRI has the ability to easily and noninvasively quantify regional gas uptake by the lung parenchyma and blood.

4.2 Hyperpolarized Xe-129 Dissolved-Phase MRI

Gas uptake by lung parenchyma and red blood cells can be assessed by Xe-129 MRI. Upon inhalation, the majority of Xe-129 gas resides in the airspace (gas phase), but there is still 1–2% dissolved in the lung parenchyma, plasma and blood (dissolved phase) [92], following the same physical gas-transfer pathway as oxygen does to reach the red blood cells in the pulmonary capillary bed (Figure 4.1). The dissolved-phase and gaseous xenon atoms continually exchange driven by diffusion in a dynamic equilibrium. The atoms in different compartments have distinctly different resonance frequencies, permitting gas uptake and exchange to be assessed using hyperpolarized Xe-129 MRI. Although the fraction of inhaled xenon dissolved in the lung parenchyma and blood is small, three spectral peaks can still be observed in whole lung spectrum, associated with different compartments: airspaces, lung tissue and red blood cells (Figure 4.2) [38, 93, 94, 91, 89]. The quantitative characteristics of the process of gas

exchange and uptake are determined by parameters of physiological relevance, such as the thickness of the blood-gas barrier [88], the ratio of the functional tissue volume to alveolar volume [95], and the surface-to-volume ratio [96]. By measuring this progress, we can acquire information on the functional status of healthy and diseased lungs.

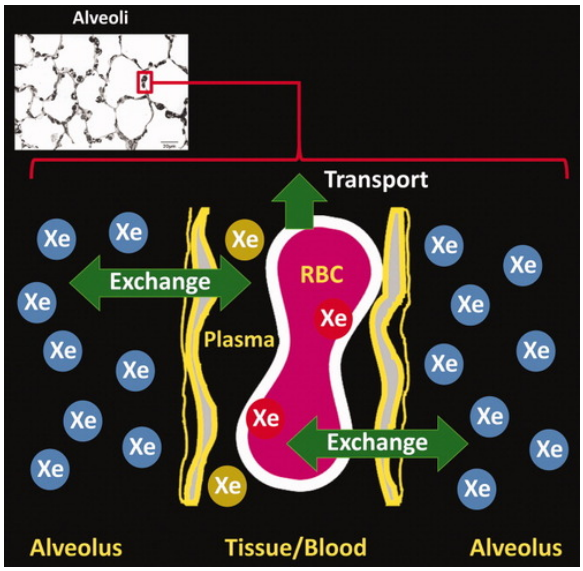

Figure 4.1: The exchange of Xe-129 between alveoli, tissue and red blood cells. Reprinted from [38].

Based on this, a three-dimensional, multi-echo, radial-trajectory pulse sequence was developed to obtain ventilation (gaseous Xe-129), tissue, and red blood cell (RBC) images in a breath-hold acquisition of less than 20 seconds [4]. Through these images, Xe-129 signal ratios (total dissolved-Xe-129-to-gas, tissue-to-gas, RBC-to-gas and RBC-to-tissue) can be calculated for quantitative regional comparisons [4].

These ratios are closely related to important lung physiological factors: the RBC-to-gas ratio represents the overall gas exchange efficiency from lung airspaces to the blood, similar to what DLCO measures globally. The tissue-to-gas ratio mainly reflects tissue density and alveolar surface-area-to-volume ratio. The RBC-to-tissue ratio is affected by pulmonary perfusion and gas-blood barrier thickness.

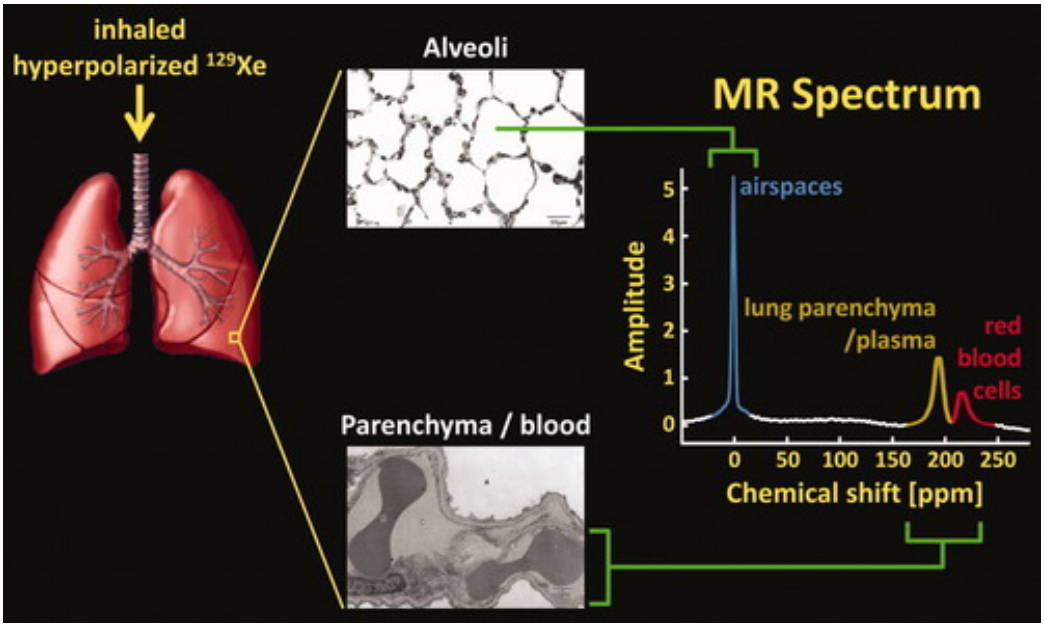

Figure 4.2: Distribution of inhaled Xe-129 in the lung and its MR spectrum. Reprinted from [38].

4.3 Current Issues and the Variability in Protocol

Although Xe-129 dissolved-phase MRI provides valuable information in assessing lung gas uptake, it encounters an issue – the lack of standardization. Each institution has its own protocol and workflow, there is not a unified protocol for dissolved-phase imaging [55, 4, 56]. Therefore, the results obtained from one institution are meaningless in a different institution. One of the parameters that cannot be ignored is the lung volume. As mentioned in Section 1.1.2, lung volume is in continuous change during respiration. Previous studies have shown a strong dependence of gas uptake measures on lung inflation level [90, 55]. In the next section, we explored the relationships between the lung inflation level when MRI is taken and the gas uptake ratios we acquired through corresponding images.

Chapter 5

The Effects of Lung Inflation Levels on the Results of the Dissolved-Phase MRI

5.1 Introduction

Previous studies showed that gas uptake ratios acquired from hyperpolarized Xe-129 MRI were remarkably affected by the level of lung inflation at which the MRI data was acquired during a single breath-hold [4, 90, 55, 89]. Specifically, the ratios would decrease as lung inflation increased [90, 55, 89]. This might lead to unreasonable results when evaluating lung function of subjects under different inflation levels. Thus, it's essential to investigate the quantitative relationship between the two. With that, better control over lung inflation in future experiments could be realized and normalized gas uptake measurements could be acquired.

In this study, we systematically investigated the change of gas uptake measured from Xe-129 dissolved-phase MRI upon different lung inflation levels. We assumed there are inverse correlations between gas uptake ratios and lung inflation level. In

the work described below, subjects underwent a combined Xe-129 dissolved-phase [4] and proton MRI acquisition in a single breath-hold, to get both gas uptake results and lung volumes. Images were acquired under three different lung inflation levels: 1.) total lung capacity (TLC); one-third of forced vital capacity (1/3 FVC); and 3.) residual volume (RV) (COPD patients usually have higher RV due to hyperinflation). Statistical analysis was performed to explore the correlations between gas uptake ratios and lung volume.

5.2 Materials and Methods

5.2.1 Human Subjects

The studies were conducted under U.S. Food and Drug Administration IND Application for MR imaging with hyperpolarized Xe-129, and the study protocol was approved by the University of Virginia's IRB. All human subjects signed informed consent after being explained the details of study procedure prior to the studies.

The study group was composed of 12 healthy, non-smoking subjects and 5 COPD subjects (1 current smoker and 4 former smokers). The healthy subjects were separated into a younger group (5 subjects) aged from 20 to 27 and an older group (7 subjects) aged from 44 to 70 matching to COPD group aged from 56 to 80. Spirometry was performed to each subject immediately before MRI scan to evaluate their pulmonary function and acquire their FVC. The demographics and pulmonary function test results are shown in Table 5.1.

Per IND requirements, 12-lead electrocardiography (HP Pagewriter XLi; Hewlett Packard Co., Palo Alto, CA) was performed in subjects 40 yo or older immediately before and after MR imaging. Female subjects received a urine pregnancy test before imaging and were excluded from participation if pregnant. All studies were supervised by physicians.

Table 5.1: Demographics and baseline spirometry results. HY represents healthy younger subjects, HO represents healthy older subjects, and C represents COPD subjects. *current smoker, **COPD and lung cancer.

Subject	**Age (yo)**	**Gender**	FEV_1 **(%Pred)**	$FEV_1/FVC(\%)$
HY1	27	F	107	83
HY2	23	F	105	83
HY3	24	F	103	82
HY4	20	F	96	94
HY5	20	F	91	81
HO1	60	F	99	84
HO2	70	F	99	84
HO3	64	F	107	71
HO4	49	F	78	73
HO5	60	F	105	74
HO6	52	F	113	80
HO7	44	F	104	84
C1*	56	F	88	65
C2**	57	M	38	37
C3	60	M	43	34
C4	80	F	84	72
C5	74	M	87	60

5.2.2 MR Measurements

MR acquisitions were performed using a 1.5T commercial whole-body MR scanner (Avanto; Siemens Medical Solutions, Malvern, PA) equipped with the multinuclear imaging option. A flexible, circularly-polarized, vest-shaped chest RF coil (Clinical MR Solutions, Brookfield, WI) blocked at the proton resonance frequency was used for all Xe-129 acquisitions. Each subject was positioned supine on the scanner table with the RF coil around the chest. Breath-hold scout images were obtained using conventional proton MRI for positioning of the Xe-129 acquisitions. Next, the subject inhaled a gas mixture containing approximately 200 mL of hyperpolarized Xe-129 gas from maximum expiration, and a breath-hold acquisition was performed for calibration of the scanner center frequency and transmitter voltage.

Three combined hyperpolarized Xe-129 dissolved-phase and proton MRI acquisitions were performed at three different inflation levels. The RV level acquisition was performed at the maximum expiration after inhaling a gas mixture containing 1L hyperpolarized Xe-129 and nitrogen from maximum expiration. For 1/3 FVC acquisition, subject inhaled gas from maximum expiration to a total volume of one-third of the subject's FVC as determined by spirometry. The TLC acquisition was performed after inhaling the gas mixture as much as possible.

Parameters used in the Xe-129 acquisitions were same as described in [4] (acquisition time 11 s), except for a lower spatial resolution (15.2 x 15.2 x 17.6 mm^3) to ensure sufficient signal-to-noise ratio. Three ratio maps (tissue-to-gas, RBC-to-gas and RBC-to-tissue) were generated from dissolved-phase MRI for quantitative comparison among subjects (Figure 5.1). Meanwhile, four gas uptake ratios were calculated: tissue-to-gas, RBC-to-gas, total dissolved-phase-to-gas (DP-to-gas) and RBC-to-tissue. A 3-D proton gradient-echo sequence was used to measure lung volume following the dissolved-phase acquisition in the same breath-hold (Figure 5.1).

Two additional proton image sets were acquired independently before or after the dissolved-phase acquisitions to measure TLC and RV. Proton image resolution was 3.9 x 3.9 x 3.9 mm^3, and the acquisition time was 4 seconds.

5.2.3 Data Analysis

Four gas uptake ratios were included in this study: tissue-to-gas, RBC-to-gas, total DP-to-gas, RBC-to-tissue. We performed Friedman tests to see whether gas uptake ratios differ among three lung inflation levels. Multiple comparisons were performed when the result of Friedman test was significant. Then we assumed there were inversely proportional relationships between gas uptake measures and normalized lung volume by TLC in healthy subjects. To test this assumption, linear regressions were applied. Healthy subjects were analyzed within two groups (younger and older). The

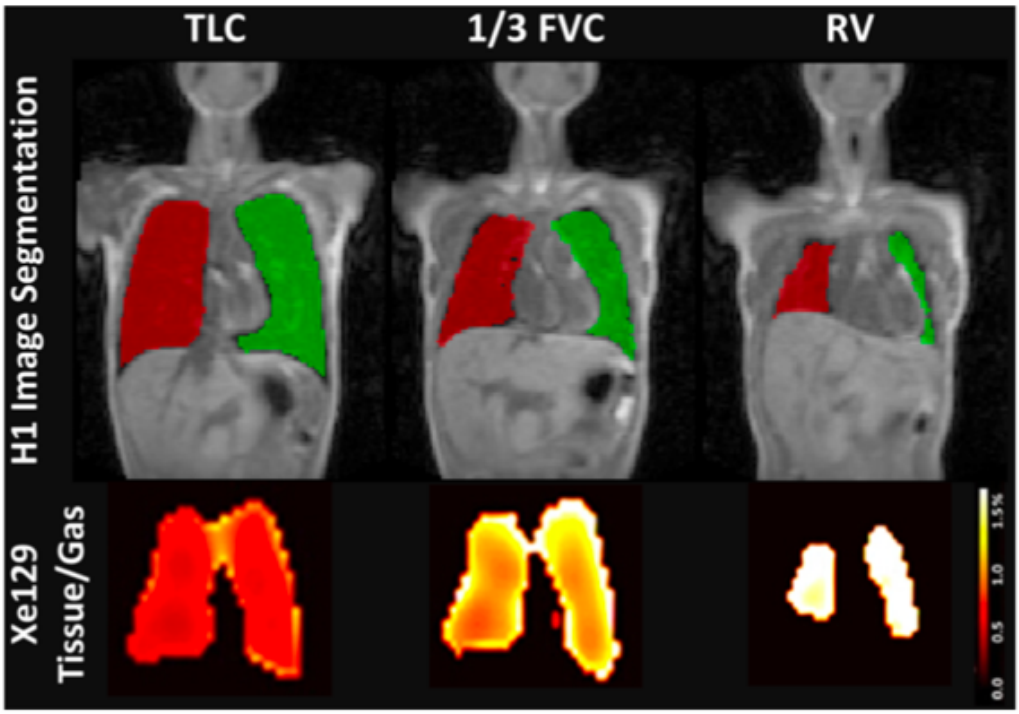

Figure 5.1: Results from the combined Xe-129 dissolved-phase and proton acquisition in a healthy subject. The first row shows coronal proton images acquired at three inflation levels and the segmented lung regions (red: right lung, green: left lung). The second row shows the corresponding measured tissue-to-gas ratio maps. Higher ratios were measured at lower lung inflation levels, as expected.

coefficient of determination r^2 and the slope of regression line k were evaluated for each group.

We assumed a similar linearity in COPD subjects. However, because of the great variance of disease among subjects (COPD GOLD stage 1 to 3), regression analysis was not suitable for COPD group. Instead, we evaluated the linearity by predicting the gas uptake values measured at intermediate inflation level (i.e., 1/3 FVC) based on those at the highest (i.e., TLC) and the lowest (i.e., RV) inflation levels. Relative errors of predicted values compared with actual values were evaluated.

Data was analyzed offline using Prism (GraphPad, San Diego, CA) and MATLAB (MathWorks, Natick, MA).

5.3 Results

5.3.1 Gas uptake measures obtained at different lung inflation levels were significantly different

Friedman tests showed all three gas uptake ratios were different among lung inflation levels ($p < 0.01$, Figure 5.2). Specifically, according to the results of Dunn's multiple comparison tests, tissue-to-gas values were significantly different among all three pairs of inflation levels (Figure 5.2 left). For RBC-to-tissue and RBC-to-tissue, only in one or two pairs of inflation levels were significantly different. These results suggest dissolved-phase MRI is sensitive to detect the lung inflation level changes.

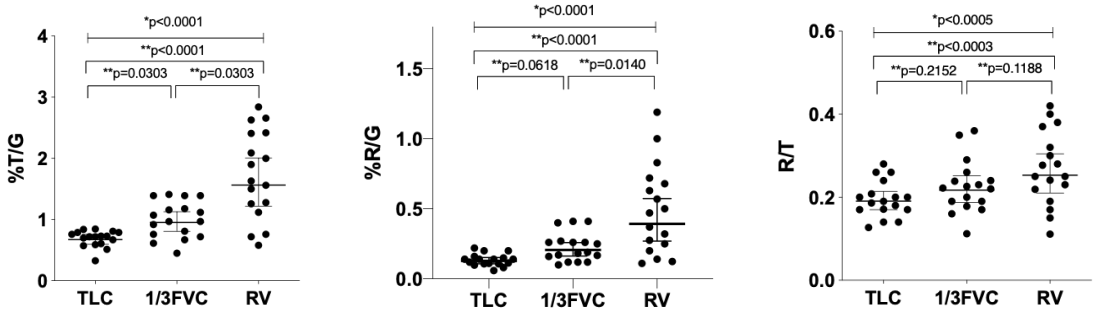

Figure 5.2: Comparisons of gas uptake ratios (left: tissue-to-gas, middle: RBC-to-gas, right: RBC-to-tissue) among three lung inflation levels. * represents p-value of Friedman tests among all three lung inflation levels. ** represents p-value of Dunn's multiple comparison tests. Significant differences were found in all three ratios among inflation levels according to the results of Friedman tests ($P < 0.0001$ for %T/G and %R/G, $P = 0.0005$ for R/T). Dunn's multiple comparison tests showed %T/G between all three pairs of inflation level were significantly different ($P = 0.03$ for 1/3 FVC vs TLC, $P < 0.01$ for RV vs TLC, $P = 0.03$ for RV vs 1/3 FVC, left). %R/G between RV vs TLC and RV vs 1/3 FVC were significantly different, but not in 1/3 FVC vs TLC ($P < 0.01$ for RV vs TLC, $P = 0.01$ for RV vs 1/3 FVC, $P = 0.06$ for 1/3 FVC vs TLC, middle). For R/T, significant difference was only found in RV vs TLC, while between 1/3 FVC vs TLC and RV vs 1/3 FVC were not ($P < 0.01$ for RV vs TLC, $P = 0.22$ for 1/3 FVC vs TLC, $P = 0.12$ for RV vs 1/3 FVC, right).

5.3.2 Strong inverse relationships between lung inflation level and gas uptake measures were found for healthy subjects

To quantitatively analyze the effects of lung inflation level at which the MRI scan was taken, we normalized lung volumes by subject's TLC determined from the independent proton MR image. We found very strong correlations between tissue-to-gas, RBC-to-gas and total DP-to-gas ratios vs lung volume for both younger and older groups ($r <= -0.78$, $p < 0.01$, Table 5.2). These measures involve the process that gas in alveolar diffusion into red blood cells determined by the surface-area-to-volume ratio of alveolar. As the lungs inflating, more xenon gas can be detected, the volume of gas in alveolar increases, then the surface-area-to-volume ratio decreases, leading to decreased gas uptake ratios. Linear regression results showed inversely proportional relationships between these ratios and normalized lung volume ($r^2 > 0.6$, Table 5.2, Figure 5.3).

RBC-to-tissue ratio, however, didn't show very strong correlation vs inflation level as the other ratios did, especially for the older subjects. This could be caused by changes in lung blood volume and/or pulmonary venous flow due to changes of the transpulmonary pressure, consistent with the literature [97]. However, an inverse changing trend was still observed in our study (Figure 5.3 lower right).

5.3.3 Younger people had higher gas uptake than older people at the same lung inflation level

Slopes of regression lines were calculated to compare younger and older healthy subjects (Table 5.2, Figure 5.3). The slopes of all four ratios in younger group were steeper than those in older group. This means younger subjects had higher gas uptake than older subjects at the same lung inflation level. Previously, hyperpolarized

Table 5.2: Regression analysis between gas uptake ratios and lung volume. Pearson correlation coefficient r, coefficient of determinate r^2, significance p and slope k of each group.

		%T/G	**%R/G**	**Total DP/G**	**R/T**
Younger	r	-0.94	-0.91	-0.93	-0.85
	r^2	0.88	0.83	0.87	0.73
	p	< 0.0001	< 0.0001	< 0.0001	< 0.0001
	k	-2.87	-1.24	-4.11	-0.25
Older	r	-0.88	-0.78	-0.86	-0.46
	r^2	0.77	0.61	0.75	0.21
	p	< 0.0001	< 0.0001	< 0.0001	0.0374
	k	-2.34	-0.61	-2.95	-0.09

He-3 diffusion MRI studies have shown that the He-3 apparent diffusion coefficient (ADC) values increase with aging [98], which could explain the lower tissue-to-gas ratio observed in older subjects – because of decreased tissue density or surface-to-volume ratios. The decrease of the RBC-to-tissue ratios with age could be caused by a decreased cardiac output [99].

5.3.4 Gas uptake measures at intermediate lung inflation level can be predicted using the highest and lowest inflation levels for COPD subjects

The inverse relationships between gas uptake measures and lung inflation level were also found in COPD group. We predicted the gas uptake ratios at intermediate inflation level (i.e., 1/3 FVC) using the values at the highest (i.e., TLC) and lowest (i.e., RV) inflation volumes. The relative errors of the predicted values compared with the actually acquired values were calculated. The mean and standard deviation of the absolute values of relative errors for the predicted tissue-to-gas, RBC-to-gas, total DP-to-gas and RBC-to-tissue values were $7.68\% \pm 6.51\%$, $9.23\% \pm 6.91\%$, $8.11\% \pm 5.60\%$

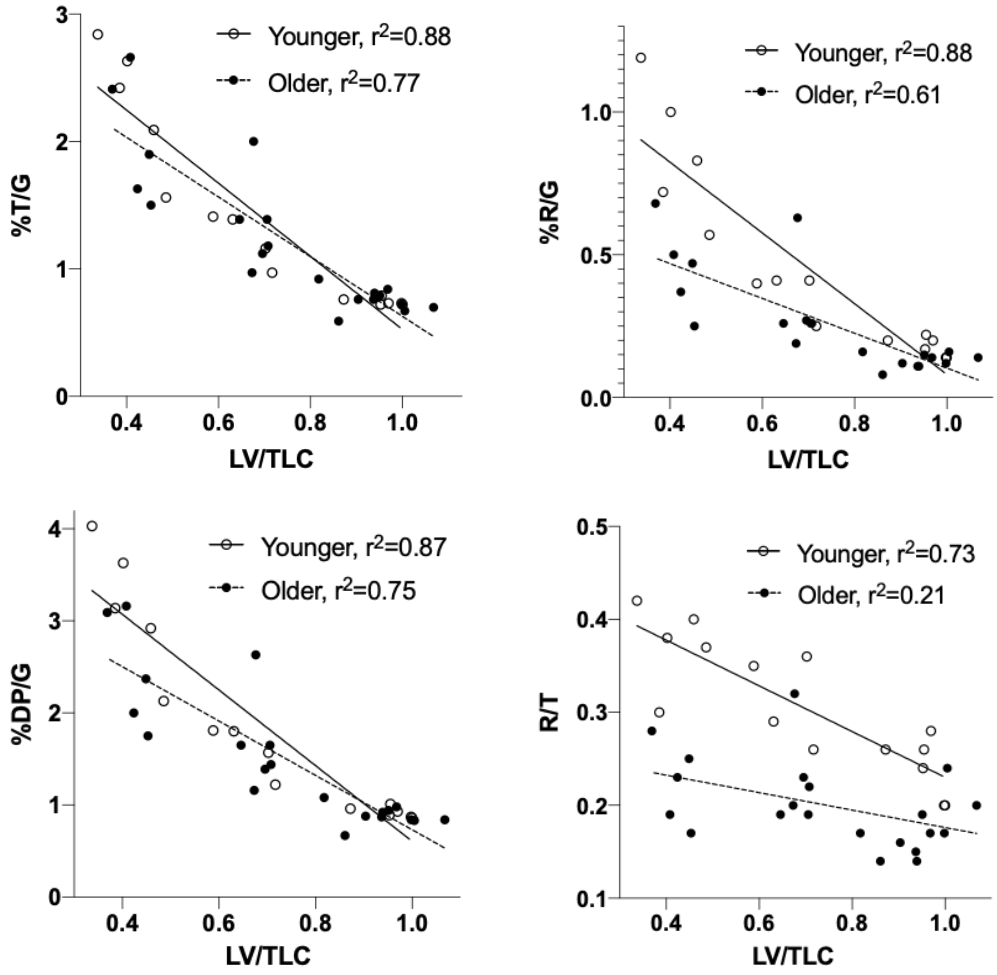

Figure 5.3: Linear regressions between gas uptake ratios (upper left: tissue-to-gas, upper right: RBC-to-gas, lower left: total DP-to-gas, lower right: tissue-to-gas) vs normalized lung volume by TLC. Healthy subjects were divided into two groups (younger and older).

and $6.63\% \pm 3.09\%$, respectively. These relatively small predicting errors suggested similar linear relationships also exist in COPD patients.

5.4 Conclusion

Significant variations of the dissolved-phase results were found from the smallest values with TLC to largest with RV. Normalization of the dissolved-phase lung volume to

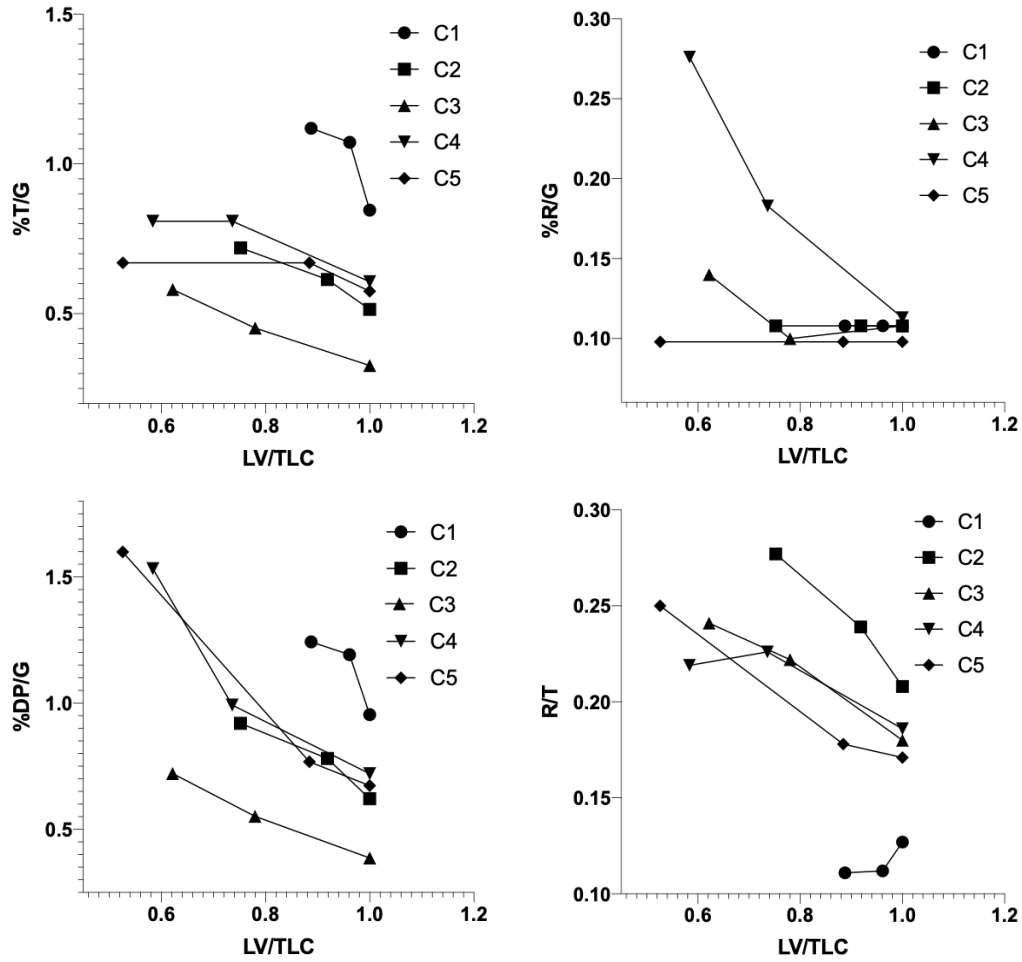

Figure 5.4: Gas uptake ratios (upper left: tissue-to-gas, upper right: RBC-to-gas, lower left: total DP-to-gas, lower right: tissue-to-gas) vs normalized lung volume in COPD subjects.

TLC substantially mitigated this variation. Strong inverse relationships were found between gas uptake ratios and normalized lung volume. This normalization strategy can be possibly exploited to assist data analyses involving multiple centers with variably MRI techniques.

Chapter 6

Lobar Analysis of Gas Uptake and the Effects of Lung Inflation Level

6.1 Introduction

According to the results in Section 3.3.3, ventilation can be heterogeneous among individual lobes, and more ventilation defects are usually observed in upper lobes. In this chapter, regional distribution of gas uptake measured by hyperpolarized Xe-129 MRI is described among different lobes. In addition, based on the results from Chapter 5, we found that dissolved-phase MRI has close association with lung inflation level. Influence of different inflation levels on each lobe will be further interrogated in this chapter. The lobar analysis of gas uptake results would provide further understanding of human lung gas exchange and help to standardize the quantitative measurements of dissolved-phase MRI.

6.2 Materials and Methods

Human subjects and MRI protocol used in this study are identical as described in Chapter 5.

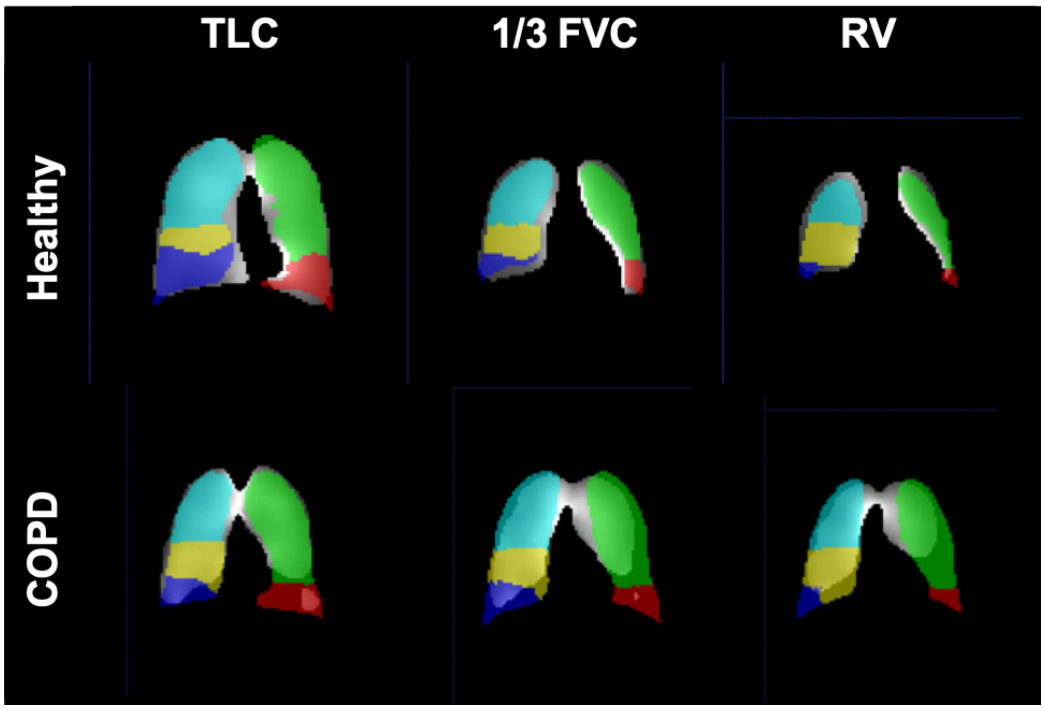

Figure 6.1: Lobar segmentation of tissue-to-gas images under different lung inflation levels. Each column represents the same inflation level (left: TLC, middle: 1/3 FVC, right: RV). Each row represents one subject (upper: healthy young subject, slice #26, lower: COPD subject, slice #41).

6.2.1 Image Processing

Proton images in the dissolved-phase acquisitions were used to measure lung volumes at breath-hold. These images were segmented obtain whole lung masks using method described in [5] and adjusted manually by scientist with abundant experiences in pulmonary MRI. Whole lung masks were further segmented using multi-atlas label fusion approach [70] to get lobar segmentation. Because proton images were acquired in the same breath-hold as Xe-129 images, these segmented masks can be directly applied to the Xe-129 images and provide lobar information about lung function accordingly. (Figure 6.1)

6.2.2 Data Analysis

Friedman tests were performed to see whether gas uptake ratios under same lung inflation level were different among lobes. Multiple comparisons were performed when the result of Friedman test was significant. Then we assumed that there were inversely proportional relationships between gas uptake measures and normalized lung volume in each lobe for healthy subjects. To test this assumption, linear regressions were applied. Healthy subjects were analyzed within two groups (younger and older). The coefficient of determination r^2 and the slope of regression line k were evaluated for each group. For COPD subjects, because of the high variance of diseases, linear regression was not performed. We only plot gas uptake ratios vs normalized lung volume to analyze this correlation qualitatively.

To further explore the association between gas uptake measures and lung inflation level in different lobes, we calculated the slopes of linear regression lines for each lobe of each subject. Friedman tests were performed to see whether these five lobes had the same slopes of change in gas uptake in response to the change of lung volumes for both healthy and COPD groups.

Data was analyzed offline using Prism (GraphPad, San Diego, CA).

6.3 Results

6.3.1 Gas uptake ratios under same lung inflation level were significantly different among lobes

According to the results of Friedman tests, all three gas uptake ratios (tissue-to-gas, RBC-to-tissue, RBC-to-tissue) were significantly different in different lobes under the same lung inflation level ($p < 0.05$, Figure 6.2). Dunn's multiple comparisons showed

gas uptake ratios in middle right lobe were very likely smaller compared with other lobes.

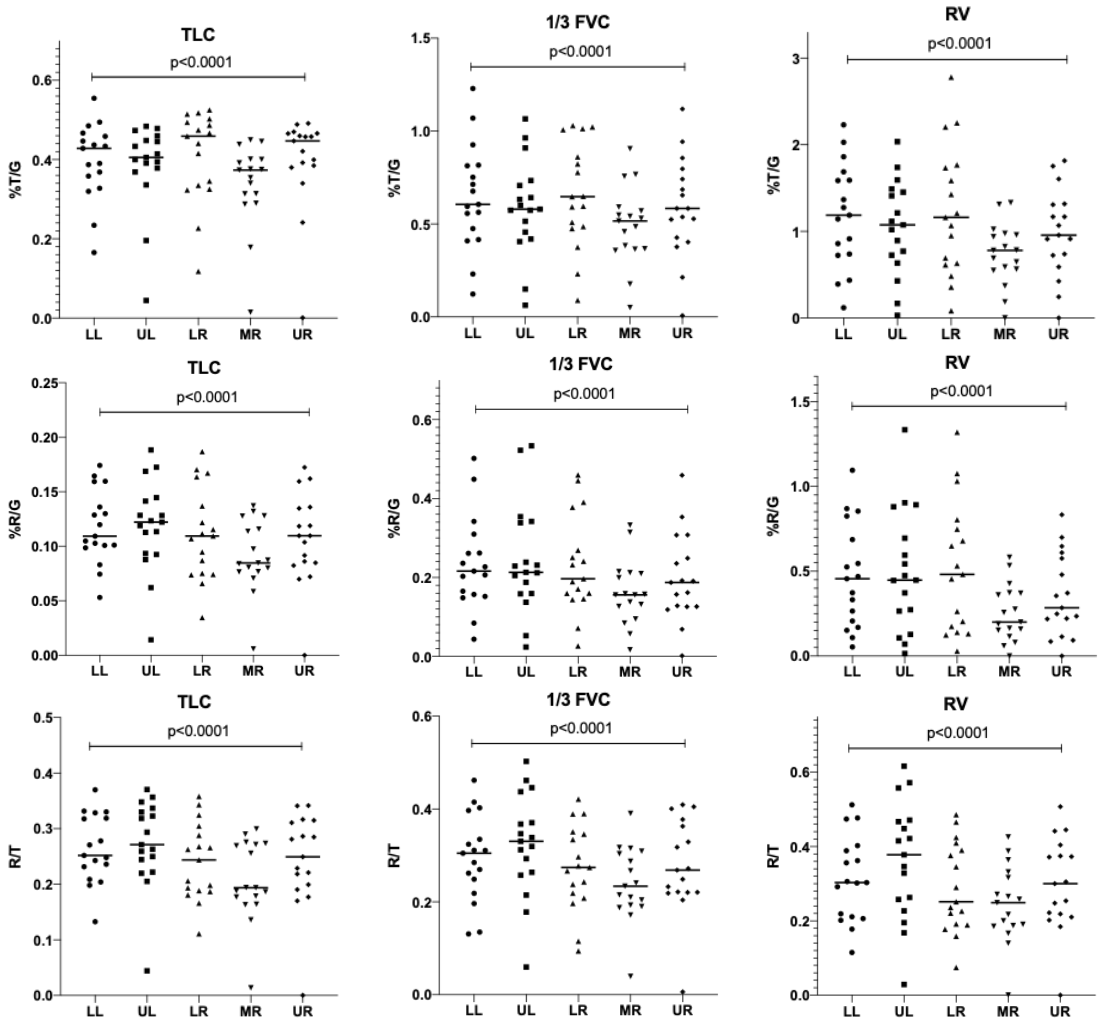

Figure 6.2: Comparisons of gas uptake ratios (row 1: tissue-to-gas, row 2: RBC-to-gas, row 3: RBC-to-tissue) among five lung lobes under three lung inflation levels (left: TLC, middle: 1/3 FVC, right: RV). Significant differences were found in all three ratios among lobes according to the results of Friedman tests ($P < 0.0001$ for all tests).

6.3.2 Strong inverse relationships between gas uptake ratios and lung volume still existed in each lobe

Very strong inverse correlations between gas uptake ratios in each lobe and lung volume were found for both healthy younger and older subjects, which consisted with the results in global analysis. Linear regression results showed inversely proportional relationships between these ratios in each lobe and normalized lung volume ($r^2 > 0.6$, Table 6.1, Figure 6.3). Younger subjects still have higher gas uptake than older subjects under the same inflation level in each lobe, shown as steeper regression lines in Figure 6.3.

Table 6.1: Regression analysis between tissue-to-gas value and lung volume. Coefficient of determinate r^2, significance p and slope k of each group.

		Lower Left	**Upper Left**	**Lower Right**	**Middle Right**	**Upper Right**
Younger	r^2	0.89	0.88	0.80	0.84	0.82
	p	< 0.0001	< 0.0001	< 0.0001	< 0.0001	< 0.0001
	k	-2.44	-2.03	-2.64	-1.24	-1.78
Older	r^2	0.78	0.78	0.75	0.62	0.71
	p	< 0.0001	< 0.0001	< 0.0001	< 0.0001	< 0.0001
	k	-1.70	-1.50	-1.92	-0.79	-1.31

Inverse relationships were also found in COPD subjects in each lobe. Because of the variation of diseases, linear regressions were not performed. However, the decreasing trend of gas uptake measures in respond to the increased lung inflation level were still observed in Figure 6.4.

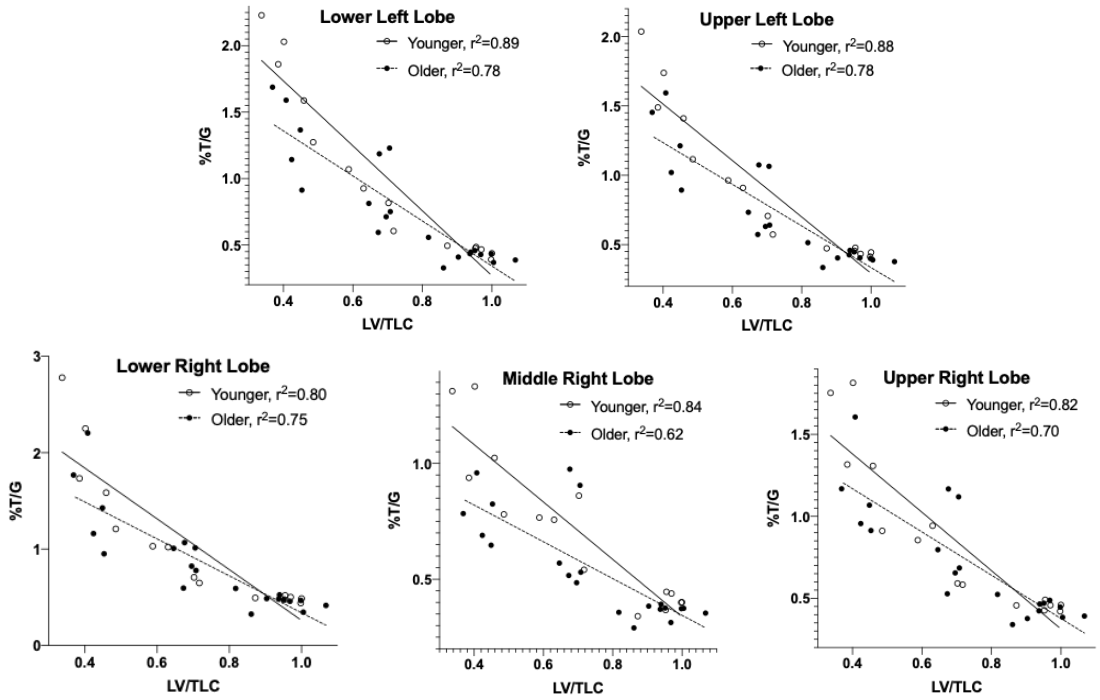

Figure 6.3: Linear regressions between tissue-to-gas value vs normalized lung volume by TLC in each lobe of healthy subjects. Upper left: lower left lobe, upper right: upper left lobe, lower left: lower right lobe, lower middle: middle right lobe, lower right: upper right lobe. Healthy subjects were divided into two groups (younger: solid line, older: dashed line). Younger groups had steeper slopes than older groups.

6.3.3 The rates of change of gas uptake ratios in response to the change of lung inflation level in healthy subjects were significantly different among different lobes, but not in COPD patients

The slopes of linear regression lines of gas uptake ratio vs normalized lung volume associated with each lobe were calculated for each subject and shown in Table 6.2. Within each subject, the slopes associated with 5 lobes were not statistically identical ($p > 0.05$, Table 6.2). Friedman test showed the slopes of 5 lobes in all healthy subjects were significantly different ($p < 0.05$, Figure 6.5 upper right). Dunn's multiple comparisons indicated except middle right lobe, there were no significant differences

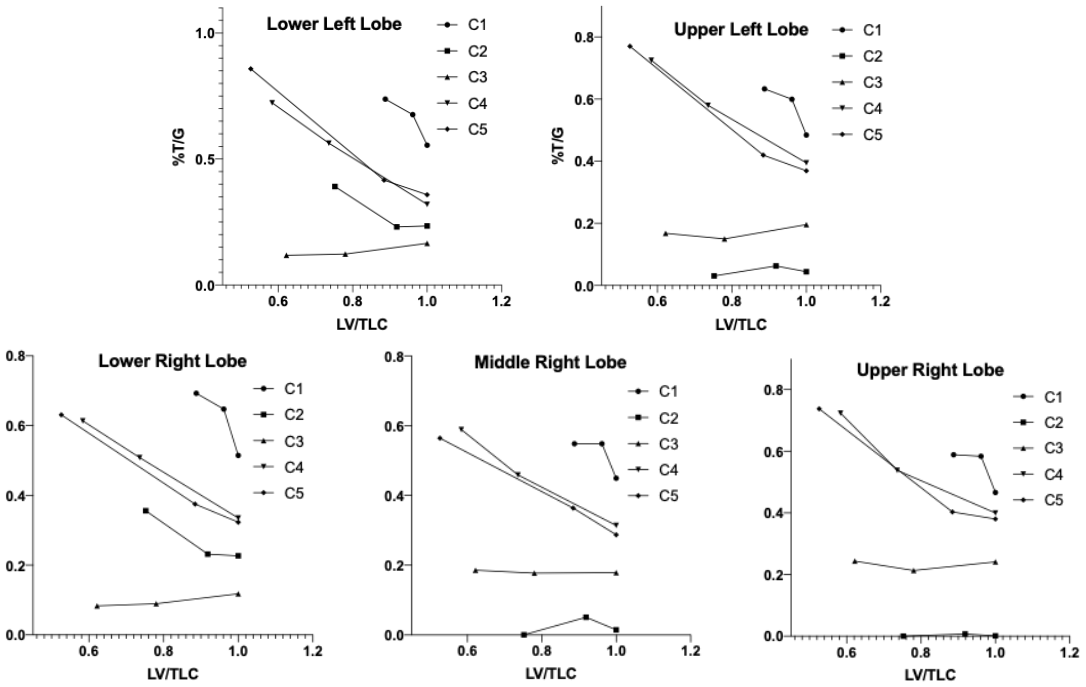

Figure 6.4: Tissue-to-gas value vs normalized lung volume by TLC in each lobe of COPD subjects. Upper left: lower left lobe, upper right: upper left lobe, lower left: lower right lobe, lower middle: middle right lobe, lower right: upper right lobe.

between the other lobes ($p >= 0.05$, Figure 6.5 upper right). Middle right lobe showed to have the least sensitivity to the change of lung volume in terms of measured gas uptake ratios. COPD subjects, however, showed similar slopes among different lobes ($p < 0.05$, Figure 6.5 lower right).

6.4 Conclusion

Gas uptake ratios were significantly different among lobes, which indicates the existence of gas uptake heterogeneity. The inverse correlations between gas uptake measures and lung volume were also found in each lobe for both healthy and COPD subjects. In healthy subjects, this correlation was further proved to be proportional. This result is consistent with the conclusion we made for global measurements in Chapter 5.

Table 6.2: The slopes of linear regression lines of tissue-to-gas vs normalized lung volume by TLC of each lobe in healthy subjects. Upper: healthy subjects, lower: COPD subjects. Left: linear regressions of tissue-to-gas vs normalized lung volume of 5 lobes in one subject. Right: the slopes of tissue-to-gas vs normalized lung volume in each lung lobe of all healthy/COPD subjects. Except the middle right lobe, slopes were not significantly different among other lobes. Slopes were not significantly different among 5 lobes in COPD subjects ($p = 0.2052$).

	Lower Left	**Upper Left**	**Lower Right**	**Middle Right**	**Upper Right**	**p-value (Are the slopes equal?)**
HY1	-2.85	-2.60	-3.70	-1.42	-2.10	0.36
HY2	-2.08	-1.76	-1.99	-1.10	-1.50	0.63
HY3	-2.44	-1.79	-2.15	-0.89	-1.49	0.51
HY4	-1.81	-1.49	-1.66	-0.96	-1.08	0.13
HY5	-2.54	-2.08	-2.81	-1.50	-2.18	0.80
HO1	-0.97	-0.59	-0.73	0.20	-0.65	0.10
HO2	-0.91	-0.89	-0.91	-0.81	-0.92	0.99
HO3	-2.03	-2.06	-3.04	-1.13	-1.94	0.48
HO4	-2.65	-2.15	-2.21	-1.81	-2.41	0.10
HO5	-1.88	-1.58	-1.93	-0.90	-1.42	0.06
HO6	-1.69	-1.47	-1.74	-0.50	-1.13	0.16
HO7	-2.15	-1.76	-2.25	-0.71	-1.22	0.17
C1	-1.52	-1.21	-1.46	-0.76	-0.95	0.91
C2	-0.68	0.08	-0.55	0.09	0.01	0.05
C3	0.13	0.08	0.09	-0.02	0.00	0.47
C4	-0.96	-0.78	-0.67	-0.65	-0.75	0.27
C5	-1.10	-0.88	-0.67	-0.58	-0.80	0.10

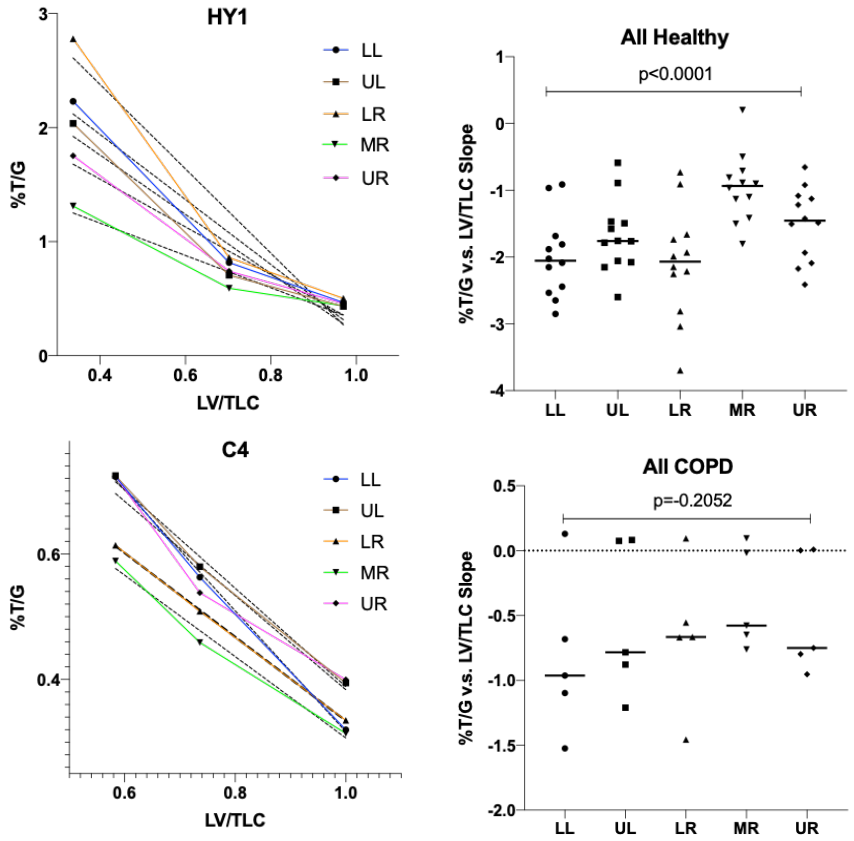

Figure 6.5: The slopes of linear regression lines of tissue-to-gas vs normalized lung volume by TLC of each lobe in healthy subjects. Upper: healthy subjects, lower: COPD subjects. Left: linear regressions of tissue-to-gas vs normalized lung volume of 5 lobes in one subject. Slopes were not significantly identical ($p = 0.36$ for healthy, $p = 0.27$ for COPD). Right: the slopes of tissue-to-gas vs normalized lung volume in each lung lobe of all healthy/COPD subjects. Slopes were significantly different among 5 lobes in healthy subjects ($p < 0.0001$). Specifically, the slopes between lower left vs middle right and lower right vs middle right were significantly different ($p < 0.0001$ for both pairs). Slopes were not significantly different among 5 lobes in COPD subjects ($p = 0.2052$).

The association between gas uptake measures and lung inflation level in individual lobes were also investigated. Within each subject, the rates of change of gas uptake ratios in respond to the changes in lung inflation level were not the same in different lobes. When investigate all healthy subjects together, this difference still existed. However, no differences were shown among all COPD subjects.

Chapter 7

Discussion and Future Work

In this work, we illustrated the application of hyperpolarized Xe-129 MRI in evaluating lung airflow and gas uptake by lung tissue and red blood cells. We summarized findings of ventilation defects in healthy subjects by quantifying unventilated percentage using deep learning. We also explored the relationships between global and regional gas uptake measures and lung volume at breath-hold. These results provide valuable reference in the clinical application of hyperpolarized Xe-129 MRI.

There is still a lot of work can be done in the future. For example, in this work, we showed that the gas uptake measured in older healthy subjects were significantly lower than those in younger healthy subjects. With increasing number of collected data, we may be able to also establish a reference line, like we did for the ventilation data in healthy subjects. By doing this, we can further identify whether the gas uptake results that we obtained from patients are in the normal range. Furthermore, we can extend this reference line to different regions of the lung using the image analysis tools that we illustrated in this work.

References

[1] Melonie Heron. Deaths: Leading causes for 2016. *National Vital Statistics Reports*, 67(6), Jul 2018.

[2] J R MacFall, H C Charles, R D Black, H Middleton, J C Swartz, B Saam, B Driehuys, C Erickson, W Happer, G D Cates, G A Johnson, and C E Ravin. Human lung air spaces: potential for mr imaging with hyperpolarized he-3. *Radiology*, 200(2):553–558, 1996. PMID: 8685356.

[3] H U Kauczor, D Hofmann, K F Kreitner, H Nilgens, R Surkau, W Heil, A Potthast, M V Knopp, E W Otten, and M Thelen. Normal and abnormal pulmonary ventilation: visualization at hyperpolarized he-3 mr imaging. *Radiology*, 201(2):564–568, 1996. PMID: 8888259.

[4] Kun Qing, Kai Ruppert, Yun Jiang, Jaime Mata, G Wilson Miller, Yun Shim, Chengbo Wang, Iulian C Ruset, F William Hersman, Talissa A Altes, and John Mugler. Regional mapping of gas uptake by blood and tissue in the human lung using hyperpolarized xenon-129 mri. *Journal of magnetic resonance imaging : JMRI*, 39, 02 2014.

[5] Nicholas J. Tustison, Brian B. Avants, Zixuan Lin, Xue Feng, Nicholas Cullen, Jaime F. Mata, Lucia Flors, James C. Gee, Talissa A. Altes, III John P. Mugler, and Kun Qing. Convolutional neural networks with template-based data augmentation for functional lung image quantification. *Academic Radiology*, 26(3):412 – 423, 2019. Special Issue: Pulmonary Functional Imaging.

[6] Ashish Kumar. Clinical anatomy of lungs, 2017.

[7] Mohamed Faisal Lutfi. The physiological basis and clinical significance of lung volume measurements. *Multidisciplinary Respiratory Medicine*, 12(1):3, Feb 2017.

[8] Wikipedia contributors. Lung volumes — Wikipedia, the free encyclopedia, 2019. [Online; accessed 23-April-2019].

[9] Carmela Maiolo, Ehab Mohamed, and M G Carbonelli. Body composition and respiratory function. *Acta Diabetologica*, 40 Suppl 1:S32–8, Oct 2003.

[10] OpenStax. *Anatomy and Physiology*, chapter 22. OpenStax, 2019.

[11] Asthma Education National and Program Prevention. Expert panel report 3 (epr-3): guidelines for the diagnosis and management of asthma-summary report 2007. *The Journal of allergy and clinical immunology*, 120(5 Suppl):S94, 2007.

[12] Eduard E de Lange, Talissa A Altes, James T Patrie, John D Gaare, Jeffrey J Knake, John P Mugler III, and Thomas A Platts-Mills. Evaluation of asthma with hyperpolarized helium-3 mri: correlation with clinical severity and spirometry. *Chest*, 130(4):1055–1062, 2006.

[13] B.R. Celli, W. MacNee, A. Agusti, A. Anzueto, B. Berg, A.S. Buist, P.M.A. Calverley, N. Chavannes, T. Dillard, B. Fahy, A. Fein, J. Heffner, S. Lareau, P. Meek, F. Martinez, W. McNicholas, J. Muris, E. Austegard, R. Pauwels, S. Rennard, A. Rossi, N. Siafakas, B. Tiep, J. Vestbo, E. Wouters, and R. ZuWallack. Standards for the diagnosis and treatment of patients with copd: a summary of the ats/ers position paper. *European Respiratory Journal*, 23(6):932–946, 2004.

[14] Anne G Wheaton, Timothy J Cunningham, Earl S Ford, and Janet B Croft. Employment and activity limitations among adults with chronic obstructive pulmonary diseaseunited states, 2013. *MMWR. Morbidity and mortality weekly report*, 64(11):289, 2015.

[15] David M Mannino, Robert C Gagnon, Thomas L Petty, and Eva Lydick. Obstructive lung disease and low lung function in adults in the united states: data from the national health and nutrition examination survey, 1988-1994. *Archives of internal medicine*, 160(11):1683–1689, 2000.

[16] Marina Saetta, Antonino Di Stefano, Graziella Turato, Fabrizio M Facchini, Laura Corbino, Cristina E Mapp, Piero Maestrelli, Adalberto Ciaccia, and Leonardo M Fabbri. Cd8+ t-lymphocytes in peripheral airways of smokers with chronic obstructive pulmonary disease. *American journal of respiratory and critical care medicine*, 157(3):822–826, 1998.

[17] STEPHENI. RENNARD. Inflammation and repair processes in chronic obstructive pulmonary disease. *American Journal of Respiratory and Critical Care Medicine*, 160(supplement_1):S12–S16, 1999. PMID: 10556162.

[18] VICTORIVO PEINADO, JOANALBERT BARBER, PIETRO ABATE, JOSEP RAMREZ, JOSEP ROCA, SALUD SANTOS, and ROBERT RODRIGUEZ-ROISIN. Inflammatory reaction in pulmonary muscular arteries of patients with mild chronic obstructive pulmonary disease. *American Journal of Respiratory and Critical Care Medicine*, 159(5):1605–1611, 1999. PMID: 10228134.

[19] R Rodriguez-Roisin and W MacNee. Pathophysiology of chronic obstructive pulmonary disease. *European Respiratory Monograph*, 38:177, 2006.

[20] Terence C O'Shaughnessy, Tareq W Ansari, Neil C Barnes, and Peter K Jeffery. Inflammation in bronchial biopsies of subjects with chronic bronchitis: inverse

relationship of cd8+ t lymphocytes with fev1. *American journal of respiratory and critical care medicine*, 155(3):852–857, 1997.

[21] K Matsuba, JL Wright, BR Wiggs, PD Pare, and JC Hogg. The changes in airways structure associated with reduced forced expiratory volume in one second. *European Respiratory Journal*, 2(9):834–839, 1989.

[22] Denis E O'donnell, Susan M Revill, and Katherine A Webb. Dynamic hyperinflation and exercise intolerance in chronic obstructive pulmonary disease. *American journal of respiratory and critical care medicine*, 164(5):770–777, 2001.

[23] Bruce H. Culver, Brian L. Graham, Allan L. Coates, Jack Wanger, Cristine E. Berry, Patricia K. Clarke, Teal S. Hallstrand, John L. Hankinson, David A. Kaminsky, Neil R. MacIntyre, Meredith C. McCormack, Margaret Rosenfeld, Sanja Stanojevic, and Daniel J. Weiner. Recommendations for a standardized pulmonary function report. an official american thoracic society technical statement. *American Journal of Respiratory and Critical Care Medicine*, 196(11):1463–1472, 12 2017.

[24] D. P. Tashkin, B. Celli, M. Decramer, D. Liu, D. Burkhart, C. Cassino, and S. Kesten. Bronchodilator responsiveness in patients with copd. *European Respiratory Journal*, 31(4):742–750, 2008.

[25] Gregg L Ruppel. What is the clinical value of lung volumes? *Respiratory Care*, 57(1):26–38, 2012.

[26] J. Wanger, J. L. Clausen, A. Coates, O. F. Pedersen, V. Brusasco, F. Burgos, R. Casaburi, R. Crapo, P. Enright, C. P. M. van der Grinten, P. Gustafsson, J. Hankinson, R. Jensen, D. Johnson, N. MacIntyre, R. McKay, M. R. Miller, D. Navajas, R. Pellegrino, and G. Viegi. Standardisation of the measurement of lung volumes. *European Respiratory Journal*, 26(3):511–522, 2005.

[27] Klaus Dalhoff, Santiago Ewig, et al. Adult patients with nosocomial pneumonia: epidemiology, diagnosis, and treatment. *Deutsches Ärzteblatt International*, 110(38):634, 2013.

[28] Tobias Welte. Imaging in the diagnosis of lung disease: more sophisticated methods require greater interdisciplinary collaboration. *Deutsches rzteblatt International*, 111(11):179–180, March 2014.

[29] Harvey O. Coxson, John Mayo, Stephen Lam, Giles Santyr, Grace Parraga, and Don D. Sin. New and current clinical imaging techniques to study chronic obstructive pulmonary disease. *American Journal of Respiratory and Critical Care Medicine*, 180(7):588–597, 2009. PMID: 19608719.

[30] Mark O Wielpütz, Claus P Heußel, Felix JF Herth, and Hans-Ulrich Kauczor. Radiological diagnosis in lung disease: factoring treatment options into the choice of diagnostic modality. *Deutsches Ärzteblatt International*, 111(11):181, 2014.

[31] G John Gibson, Robert Loddenkemper, Yves Sibille, and Bo Lundbäck. *European lung white book*. European Respiratory Society, 2013.

[32] Yasutaka Nakano, Shigeo Muro, Hiroaki Sakai, Toyohiro Hirai, Kazuo Chin, Mitsuhiro Tsukino, Koichi Nishimura, Harumi Itoh, Peter D Paré, James C Hogg, et al. Computed tomographic measurements of airway dimensions and emphysema in smokers: correlation with lung function. *American journal of respiratory and critical care medicine*, 162(3):1102–1108, 2000.

[33] Yasutaka Nakano, Nestor L Müller, Gregory G King, Akio Niimi, Steven E Kalloger, Michiaki Mishima, and Peter D Pare. Quantitative assessment of airway remodeling using high-resolution ct. *Chest*, 122(6):271S–275S, 2002.

[34] Sebastian Ley. Lung imaging. *European Respiratory Review*, 24(136):240–245, 2015.

[35] Jane P Ko, Scott Brandman, Joseph Stember, and David P Naidich. Dual-energy computed tomography: concepts, performance, and thoracic applications. *Journal of thoracic imaging*, 27(1):7–22, 2012.

[36] DP Schuster and T Blackwell. Lung biology in health and disease. 2005.

[37] H.-U. Kauczor, R. Surkau, and T. Roberts. Mri using hyperpolarized noble gases. *European Radiology*, 8(5):820–827, Jun 1998.

[38] John P. Mugler III and Talissa A. Altes. Hyperpolarized 129xe mri of the human lung. *Journal of Magnetic Resonance Imaging*, 37(2):313–331, 2013.

[39] F. William Hersman, Iulian C. Ruset, Stephen Ketel, Iga Muradian, Silviu D. Covrig, Jan Distelbrink, Walter Porter, David Watt, Jeffrey Ketel, John Brackett, Aaron Hope, and Samuel Patz. Large production system for hyperpolarized 129xe for human lung imaging studies. *Academic Radiology*, 15(6):683 – 692, 2008.

[40] I. C. Ruset, S. Ketel, and F. W. Hersman. Optical pumping system design for large production of hyperpolarized ^{129}Xe. *Phys. Rev. Lett.*, 96:053002, Feb 2006.

[41] Michael Salerno, Talissa A Altes, John P Mugler, Masashi Nakatsu, Hiroto Hatabu, and Eduard E de Lange. Hyperpolarized noble gas mr imaging of the lung: Potential clinical applications. *European Journal of Radiology*, 40(1):33 – 44, 2001.

[42] Shin Matsuoka, Samuel Patz, Mitchell S Albert, Yanping Sun, Rahim R Rizi, Warren B Gefter, and Hiroto Hatabu. Hyperpolarized gas mr imaging of the lung: current status as a research tool. *Journal of thoracic imaging*, 24(3):181188, August 2009.

[43] Sean Fain, Mark L. Schiebler, David G. McCormack, and Grace Parraga. Imaging of lung function using hyperpolarized helium-3 magnetic resonance imaging: Review of current and emerging translational methods and applications. *Journal of Magnetic Resonance Imaging*, 32(6):1398–1408, 2010.

[44] Yanping Sun, Brian P. O'Sullivan, John P. Roche, Ronn Walvick, Austin Reno, Dawn Baker, Joey K. Mansour, and Mitchell S. Albert. Using hyperpolarized 3he mri to evaluate treatment efficacy in cystic fibrosis patients. *Journal of Magnetic Resonance Imaging*, 34(5):1206–1211, 2011.

[45] Sean B. Fain, Frank R. Korosec, James H. Holmes, Rafael O'Halloran, Ronald L. Sorkness, and Thomas M. Grist. Functional lung imaging using hyperpolarized gas mri. *Journal of Magnetic Resonance Imaging*, 25(5):910–923, 2007.

[46] Keith W Miller, Nicholas V Reo, AJ Schoot Uiterkamp, Diane P Stengle, Thomas R Stengle, and Kenneth L Williamson. Xenon nmr: chemical shifts of a general anesthetic in common solvents, proteins, and membranes. *Proceedings of the National Academy of Sciences*, 78(8):4946–4949, 1981.

[47] Franois Pontana, Jean-Baptiste Faivre, Martine Remy-Jardin, Thomas Flohr, Bernhard Schmidt, Nunzia Tacelli, Vittorio Pansini, and Jacques Remy. Lung perfusion with dual-energy multidetector-row ct (mdct): Feasibility for the evaluation of acute pulmonary embolism in 117 consecutive patients. *Academic Radiology*, 15(12):1494 – 1504, 2008.

[48] Eric A. Hoffman and Deokiee Chon. Computed tomography studies of lung ventilation and perfusion. *Proceedings of the American Thoracic Society*, 2(6):492–498, 2005. PMID: 16352755.

[49] Hiroto Hatabu, David C Alsop, John Listerud, Mathieu Bonnet, and Warren B Gefter. T2* and proton density measurement of normal human lung parenchyma using submillisecond echo time gradient echo magnetic resonance imaging. *European journal of radiology*, 29(3):245–252, 1999.

[50] Klaus W Stock, Qun Chen, Hiroto Hatabu, and Robert R Edelman. Magnetic resonance t2 measurements of the normal human lung in vivo with ultra-short echo times. *Magnetic Resonance Imaging*, 17(7):997 – 1000, 1999.

[51] Yoshiharu Ohno, Hisanobu Koyama, Takeshi Yoshikawa, Keiko Matsumoto, Masaya Takahashi, Marc Van Cauteren, and Kazuro Sugimura. T2* measurements of 3-t mri with ultrashort tes: capabilities of pulmonary function assessment and clinical stage classification in smokers. *American Journal of Roentgenology*, 197(2):W279–W285, 2011.

[52] G. Wilson Miller, John P. Mugler III, Rui C. S, Talissa A. Altes, G. Kim Prisk, and Susan R. Hopkins. Advances in functional and structural imaging of the human lung using proton mri. *NMR in Biomedicine*, 27(12):1542–1556, 2014.

[53] Kuniyoshi Sakai, Anastacia M Bilek, Eduardo Oteiza, Ronald L Walsworth, Dilip Balamore, Ferenc A Jolesz, and Mitchell S Albert. Temporal dynamics of hyperpolarized129xe resonances in living rats, 1996.

[54] M.S. Albert and D. Balamore. Development of hyperpolarized noble gas mri. *Nuclear Instruments and Methods in Physics Research Section A: Accelerators, Spectrometers, Detectors and Associated Equipment*, 402(2):441 – 453, 1998. Proceedings of the 7th RCNP International Workshop on Polarized He Beams and Gas Targets and Their Application.

[55] S. Sivaram Kaushik, Matthew S. Freeman, Zackary I. Cleveland, John Davies, Jane Stiles, Rohan S. Virgincar, Scott H. Robertson, Mu He, Kevin T. Kelly, W. Michael Foster, H. Page McAdams, and Bastiaan Driehuys. Probing the regional distribution of pulmonary gas exchange through single-breath gas- and dissolved-phase 129xe mr imaging. *Journal of Applied Physiology*, 115(6):850–860, 2013. PMID: 23845983.

[56] S. Sivaram Kaushik, Scott H. Robertson, Matthew S. Freeman, Mu He, Kevin T. Kelly, Justus E. Roos, Craig R. Rackley, W. Michael Foster, H. Page McAdams, and Bastiaan Driehuys. Single-breath clinical imaging of hyperpolarized 129xe in the airspaces, barrier, and red blood cells using an interleaved 3d radial 1-point dixon acquisition. *Magnetic Resonance in Medicine*, 75(4):1434–1443, 2016.

[57] E. D. Bateman, S. S. Hurd, P. J. Barnes, J. Bousquet, J. M. Drazen, M. FitzGerald, P. Gibson, K. Ohta, P. O'Byrne, S. E. Pedersen, E. Pizzichini, S. D. Sullivan, S. E. Wenzel, and H. J. Zar. Global strategy for asthma management and prevention: Gina executive summary. *European Respiratory Journal*, 31(1):143–178, 2008.

[58] Jrgen Vestbo, Suzanne S. Hurd, Alvar G. Agust, Paul W. Jones, Claus Vogelmeier, Antonio Anzueto, Peter J. Barnes, Leonardo M. Fabbri, Fernando J. Martinez, Masaharu Nishimura, Robert A. Stockley, Don D. Sin, and Roberto Rodriguez-Roisin. Global strategy for the diagnosis, management, and prevention of chronic obstructive pulmonary disease. *American Journal of Respiratory and Critical Care Medicine*, 187(4):347–365, 2013. PMID: 22878278.

[59] Harpreet Ranu, Michael Wilde, and Brendan Madden. Pulmonary function tests. *The Ulster medical journal*, 80(2):84, 2011.

[60] Sylvia Verbanck, Bruce R Thompson, Daniel Schuermans, Harpal Kalsi, Martyn Biddiscombe, Chris Stuart-Andrews, Shane Hanon, Alain Van Muylem, Manuel Paiva, Walter Vincken, and Omar Usmani. Ventilation heterogeneity in the acinar and conductive zones of the normal ageing lung. *Thorax*, 67(9):789–795, 2012.

[61] JOHNL. HANKINSON, JOHNR. ODENCRANTZ, and KATHLEENB. FEDAN. Spirometric reference values from a sample of the general u.s. popula-

tion. *American Journal of Respiratory and Critical Care Medicine*, 159(1):179–187, 1999. PMID: 9872837.

[62] Paul D Robinson, Michael D Goldman, and Per M Gustafsson. Inert gas washout: theoretical background and clinical utility in respiratory disease. *Respiration*, 78(3):339–355, 2009.

[63] Sarah Svenningsen, Miranda Kirby, Danielle Starr, Harvey O Coxson, Nigel A M Paterson, David G McCormack, and Grace Parraga. What are ventilation defects in asthma? *Thorax*, 69(1):63–71, 2014.

[64] Talissa A Altes, Patrick L Powers, Jack Knight-Scott, Gary Rakes, Thomas AE Platts-Mills, Eduard E de Lange, Bennett A Alford, John P Mugler III, and James R Brookeman. Hyperpolarized 3he mr lung ventilation imaging in asthmatics: preliminary findings. *Journal of Magnetic Resonance Imaging: An Official Journal of the International Society for Magnetic Resonance in Medicine*, 13(3):378–384, 2001.

[65] Yang-Sheng Tzeng, Kenneth Lutchen, and Mitchell Albert. The difference in ventilation heterogeneity between asthmatic and healthy subjects quantified using hyperpolarized 3he mri. *Journal of Applied Physiology*, 106(3):813–822, 2009. PMID: 19023025.

[66] David M.L. Lilburn, Galina E. Pavlovskaya, and Thomas Meersmann. Perspectives of hyperpolarized noble gas mri beyond 3he. *Journal of Magnetic Resonance*, 229:173 – 186, 2013. Frontiers of In Vivo and Materials MRI Research.

[67] Hans-Ulrich Kauczor, Michael Ebert, Karl-Friedrich Kreitner, Helge Nilgens, Reinhard Surkau, Werner Heil, Dirk Hofmann, Ernst W Otten, and Manfred Thelen. Imaging of the lungs using 3he mri: preliminary clinical experience in 18 patients with and without lung disease. *Journal of Magnetic Resonance Imaging*, 7(3):538–543, 1997.

[68] Saba Samee, Talissa Altes, Patrick Powers, Eduard E de Lange, Jack Knight-Scott, Gary Rakes, John P Mugler III, Jonathan M Ciambotti, Bennet A Alford, James R Brookeman, et al. Imaging the lungs in asthmatic patients by using hyperpolarized helium-3 magnetic resonance: assessment of response to methacholine and exercise challenge. *Journal of Allergy and Clinical Immunology*, 111(6):1205–1211, 2003.

[69] Helen Marshall, Martin H Deppe, Juan Parra-Robles, Susan Hillis, Catherine G Billings, Smitha Rajaram, Andrew Swift, Sam R Miller, Joanna H Watson, Jan Wolber, et al. Direct visualisation of collateral ventilation in copd with hyperpolarised gas mri. *Thorax*, 67(7):613–617, 2012.

[70] Hongzhi Wang, Jung W. Suh, Sandhitsu R. Das, John Pluta, Caryne Craige, and Paul A. Yushkevich. Multi-atlas segmentation with joint label fusion. *IEEE Trans. Pattern Anal. Mach. Intell.*, 35(3):611–623, March 2013.

[71] Nicholas J. Tustison, Brian B. Avants, Lucia Flors, Talissa A. Altes, Eduard E. de Lange, John P. Mugler III, and James C. Gee. Ventilation-based segmentation of the lungs using hyperpolarized 3he mri. *Journal of Magnetic Resonance Imaging*, 34(4):831–841, 2011.

[72] Yann LeCun, Yoshua Bengio, and Geoffrey Hinton. Deep learning. *nature*, 521(7553):436, 2015.

[73] Luke Taylor. Improving deep learning with generic data augmentation. *2018 IEEE Symposium Series on Computational Intelligence (SSCI)*, pages 1542–1547, 2018.

[74] Jos V. Manjn, Pierrick Coup, Luis Mart-Bonmat, D. Louis Collins, and Montserrat Robles. Adaptive non-local means denoising of mr images with spatially varying noise levels. *Journal of Magnetic Resonance Imaging*, 31(1):192–203, 2010.

[75] Miranda Kirby, Mohammadreza Heydarian, Sarah Svenningsen, Andrew Wheatley, David G McCormack, Roya Etemad-Rezai, and Grace Parraga. Hyperpolarized 3he magnetic resonance functional imaging semiautomated segmentation. *Academic radiology*, 19(2):141–152, 2012.

[76] Mu He, S Sivaram Kaushik, Scott H Robertson, Matthew S Freeman, Rohan S Virgincar, H Page McAdams, and Bastiaan Driehuys. Extending semiautomatic ventilation defect analysis for hyperpolarized 129xe ventilation mri. *Academic radiology*, 21(12):1530–1541, 2014.

[77] Olaf Ronneberger, Philipp Fischer, and Thomas Brox. U-net: Convolutional networks for biomedical image segmentation. In *International Conference on Medical image computing and computer-assisted intervention*, pages 234–241. Springer, 2015.

[78] E. Shelhamer, J. Long, and T. Darrell. Fully convolutional networks for semantic segmentation. *IEEE Transactions on Pattern Analysis and Machine Intelligence*, 39(4):640–651, April 2017.

[79] J. Deng, W. Dong, R. Socher, L.-J. Li, K. Li, and L. Fei-Fei. ImageNet: A Large-Scale Hierarchical Image Database. In *CVPR09*, 2009.

[80] Brian B. Avants, Paul Yushkevich, John Pluta, David Minkoff, Marc Korczykowski, John Detre, and James C. Gee. The optimal template effect in hippocampus studies of diseased populations. *NeuroImage*, 49(3):2457 – 2466, 2010.

[81] Nicholas C. Cullen and Brian B. Avants. *Convolutional Neural Networks for Rapid and Simultaneous Brain Extraction and Tissue Segmentation*, pages 13–34. Springer New York, New York, NY, 2018.

[82] Vinod Nair and Geoffrey E. Hinton. Rectified linear units improve restricted boltzmann machines. In *Proceedings of the 27th International Conference on International Conference on Machine Learning*, ICML'10, pages 807–814, USA, 2010. Omnipress.

[83] S. K. Warfield, K. H. Zou, and W. M. Wells. Simultaneous truth and performance level estimation (staple): an algorithm for the validation of image segmentation. *IEEE Transactions on Medical Imaging*, 23(7):903–921, July 2004.

[84] Nicholas J. Tustison, Talissa A. Altes, Gang Song, Eduard E. de Lange, John P. Mugler III, and James C. Gee. Feature analysis of hyperpolarized helium-3 pulmonary mri: A study of asthmatics versus nonasthmatics. *Magnetic Resonance in Medicine*, 63(6):1448–1455, 2010.

[85] R Scott Harris, Hanae Fujii-Rios, Tilo Winkler, Guido Musch, Marcos F Vidal Melo, and José G Venegas. Ventilation defect formation in healthy and asthma subjects is determined by lung inflation. *PLoS One*, 7(12):e53216, 2012.

[86] Chingyee Tan, Kun Qing, Lukasz Myc, Jiyoung Shin, Zixuan Lin, Nicholas J. Tustison, Jamie F. Mata, Amanda Shim, Emmaline Calhoun, Fiona Bradshaw, Theresa A. Altherr, Sarah Struchen, Joanne M. Cassani, Talissa A. Altes, Huang Y, III Mugler, John P., and Yun Michael Shim. Hyperpolarized-xenon ventilation magnetic resonance imaging of healthy subjects with normal spirometry. submitted.

[87] F. J. W. Roughton and R. E. Forster. Relative importance of diffusion and chemical reaction rates in determining rate of exchange of gases in the human lung, with special reference to true diffusing capacity of pulmonary membrane and volume of blood in the lung capillaries. *Journal of Applied Physiology*, 11(2):290–302, 1957. PMID: 13475180.

[88] Bastiaan Driehuys, Gary P. Cofer, Jim Pollaro, Julie Boslego Mackel, Laurence W. Hedlund, and G. Allan Johnson. Imaging alveolar–capillary gas transfer using hyperpolarized 129xe mri. *Proceedings of the National Academy of Sciences*, 103(48):18278–18283, 2006.

[89] John P. Mugler, Talissa A. Altes, Iulian C. Ruset, Isabel M. Dregely, Jaime F. Mata, G. Wilson Miller, Stephen Ketel, Jeffrey Ketel, F. William Hersman, and Kai Ruppert. Simultaneous magnetic resonance imaging of ventilation distribution and gas uptake in the human lung using hyperpolarized xenon-129. *Proceedings of the National Academy of Sciences*, 107(50):21707–21712, 2010.

[90] Kun Qing, John P. Mugler III, Talissa A. Altes, Yun Jiang, Jaime F. Mata, G. Wilson Miller, Iulian C. Ruset, F. William Hersman, and Kai Ruppert. Assessment of lung function in asthma and copd using hyperpolarized 129xe chemical shift saturation recovery spectroscopy and dissolved-phase mri. *NMR in biomedicine*, 27(12):1490–1501, 2014.

[91] Zackary I. Cleveland, Gary P. Cofer, Gregory Metz, Denise Beaver, John Nouls, S. Sivaram Kaushik, Monica Kraft, Jan Wolber, Kevin T. Kelly, H. Page McAdams, and Bastiaan Driehuys. Hyperpolarized 129xe mr imaging of alveolar gas uptake in humans. *PLOS ONE*, 5(8):1–8, 08 2010.

[92] Kai Ruppert, James R Brookeman, Klaus D Hagspiel, and John P Mugler III. Probing lung physiology with xenon polarization transfer contrast (xtc). *Magnetic Resonance in Medicine: An Official Journal of the International Society for Magnetic Resonance in Medicine*, 44(3):349–357, 2000.

[93] John P. Mugler III, Bastiaan Driehuys, James R. Brookeman, Gordon D. Cates, Stuart S. Berr, Robert G. Bryant, Thomas M. Daniel, Eduard E. De Lange, J. Hunter Downs, Christopher J. Erickson, et al. Mr imaging and spectroscopy using hyperpolarized 129xe gas: preliminary human results. *Magnetic Resonance in Medicine*, 37(6):809–815, 1997.

[94] Kuniyoshi Sakai, Anastacia M. Bilek, Eduardo Oteiza, Ronald L. Walsworth, Dilip Balamore, Ferenc A. Jolesz, and Mitchell S. Albert. Temporal dynamics of hyperpolarized129xe resonances in living rats. *Journal of Magnetic Resonance, Series B*, 111(3):300 – 304, 1996.

[95] Isabel Dregely, John P. Mugler III, Iulian C. Ruset, Talissa A. Altes, Jaime F. Mata, G. Wilson Miller, Jeffrey Ketel, Steve Ketel, Jan Distelbrink, F.W. Hersman, and Kai Ruppert. Hyperpolarized xenon-129 gas-exchange imaging of lung microstructure: First case studies in subjects with obstructive lung disease. *Journal of Magnetic Resonance Imaging*, 33(5):1052–1062, 2011.

[96] JP Butler, RW Mair, D Hoffmann, MI Hrovat, RA Rogers, GP Topulos, RL Walsworth, and S Patz. Measuring surface-area-to-volume ratios in soft porous materials using laser-polarized xenon interphase exchange nuclear magnetic resonance. *Journal of Physics: Condensed Matter*, 14(13):L297, 2002.

[97] R Brower, Robert A Wise, C Hassapoyannes, B Bromberger-Barnea, and S Permutt. Effect of lung inflation on lung blood volume and pulmonary venous flow. *Journal of Applied Physiology*, 58(3):954–963, 1985.

[98] Talissa A. Altes, Jaime Mata, Eduard E. de Lange, James R. Brookeman, and John P. Mugler III. Assessment of lung development using hyperpolarized helium-3 diffusion mr imaging. *Journal of Magnetic Resonance Imaging*, 24(6):1277–1283, 2006.

[99] MARTIN BRANDFONBRENER, MILTON LANDOWNE, and NATHAN W. SHOCK. Changes in cardiac output with age. *Circulation*, 12(4):557–566, 1955.